



HAL
open science

Pre-eruptive excess volatiles and their relationship to effusive and explosive eruption styles in semi-plugged volcanoes

Sri Budhi Utami, Joan Andújar, Fidel Costa, Bruno Scaillet, Hanik Humaida, Simon Carn

► To cite this version:

Sri Budhi Utami, Joan Andújar, Fidel Costa, Bruno Scaillet, Hanik Humaida, et al.. Pre-eruptive excess volatiles and their relationship to effusive and explosive eruption styles in semi-plugged volcanoes. *Frontiers in Earth Science*, 2022, 10, <10.3389/feart.2022.882097>. <hal-03953763>

HAL Id: hal-03953763

<https://hal.science/hal-03953763v1>

Submitted on 24 Jan 2023

HAL is a multi-disciplinary open access archive for the deposit and dissemination of scientific research documents, whether they are published or not. The documents may come from teaching and research institutions in France or abroad, or from public or private research centers.

L'archive ouverte pluridisciplinaire **HAL**, est destinée au dépôt et à la diffusion de documents scientifiques de niveau recherche, publiés ou non, émanant des établissements d'enseignement et de recherche français ou étrangers, des laboratoires publics ou privés.



HAL Authorization



OPEN ACCESS

EDITED BY

Jacob B. Lowenstern,
United States Geological Survey,
United States

REVIEWED BY

Kayla Iacovino,
Johnson Space Center (NASA),
United States
Mike Cassidy,
University of Oxford, United Kingdom

*CORRESPONDENCE

Sri Budhi Utami,
sri.budhi.utami@gmail.com

SPECIALTY SECTION

This article was submitted to
Volcanology,
a section of the journal
Frontiers in Earth Science

RECEIVED 23 February 2022

ACCEPTED 29 July 2022

PUBLISHED 09 September 2022

CITATION

Utami SB, Andújar J, Costa F, Scaillet B,
Humaida H and Carn S (2022), Pre-
eruptive excess volatiles and their
relationship to effusive and explosive
eruption styles in semi-
plugged volcanoes.
Front. Earth Sci. 10:882097.
doi: 10.3389/feart.2022.882097

COPYRIGHT

© 2022 Utami, Andújar, Costa, Scaillet,
Humaida and Carn. This is an open-
access article distributed under the
terms of the [Creative Commons
Attribution License \(CC BY\)](https://creativecommons.org/licenses/by/4.0/). The use,
distribution or reproduction in other
forums is permitted, provided the
original author(s) and the copyright
owner(s) are credited and that the
original publication in this journal is
cited, in accordance with accepted
academic practice. No use, distribution
or reproduction is permitted which does
not comply with these terms.

Pre-eruptive excess volatiles and their relationship to effusive and explosive eruption styles in semi-plugged volcanoes

Sri Budhi Utami^{1*}, Juan Andújar², Fidel Costa^{1,3,4},
Bruno Scaillet², Hanik Humaida⁵ and Simon Carn⁶

¹Asian School of the Environment, Nanyang Technological University, Singapore, Singapore, ²Institut des Sciences de La Terre Orléans (ISTO), CNRS-Université D'Orléans-BRGM, Orléans, France, ³Earth Observatory of Singapore, Singapore, Singapore, ⁴Université Paris Cité, Institut de Physique Du Globe de Paris, CNRS, Paris, France, ⁵Balai Penyelidikan Dan Perkembangan Teknologi Kebencanaan Geologi, Yogyakarta, Indonesia, ⁶Michigan Technological University, Houghton, MI, United States

Understanding the role of various factors influencing eruption style is challenging, but it can aid in adapting different hazard mitigations and crisis responses for explosive or effusive events. Here, we focus on the role of magma storage conditions in controlling eruption styles at basaltic andesite volcanoes, and how they can be related to monitoring data. We study the cycle of explosive (1990, sub-Plinian) → effusive (2007, dome) → explosive (2014, sub-Plinian) eruptions from Kelud (Kelut) volcano, Indonesia. We conducted petrological analyses of the eruption products and phase equilibria experiments using pumice and explored a range of temperatures, pressures, oxygen fugacity, and volatile contents. We show that we can reproduce the main mineral assemblage (plagioclase ± pyroxenes ± magnetite ± amphibole ± olivine) and phenocryst content (30–50 wt%) of the magmas from the three eruptions at $T = 975 \pm 39^\circ\text{C}$, $p = 175 \pm 25 \text{ MPa}$, $f_{\text{O}_2} = \text{nickel-nickel oxide buffer}$, and about 4–6 wt% water in the melt (ca. 3 to 5 wt% and ca. 4 to 7 wt% for the 1990 and 2014 eruptions, respectively). However, geothermobarometric results also indicate that some crystals of amphibole were sourced from higher pressures. We infer from a synthesis of our data and historical observations that the high phenocryst content of the 2007 dome (~70 wt%) likely resulted from slow magma ascent toward the surface alongside progressive degassing and re-equilibration at a lower volatile content (~1 wt% water in the melt). Mass balance calculations on the sulfur budget of the 1990, 2007, and 2014 magmas show that the explosive events contained an excess fluid phase at pre-eruptive conditions, and we propose that this led to their higher explosivity compared to the 2007 dome. The accumulation of excess fluids during decadal-long repose depends on how plugged the volcanic system is, or its ability to passively release magmatic fluids, prior to eruption. Such condition could be inferred from monitoring records, including changes in gravity of the plumbing system over time, and thus contribute to better anticipate eruptive style.

KEYWORDS

experimental petrology, Kelud, Kelut, eruption style, volatiles, volcano monitoring, basaltic andesite, arc volcanoes

1 Introduction

Volcanoes can display a range of eruption styles, spanning from small phreatic events and dome growth to explosive events with tall eruptive columns. Moreover, changes can occur between consecutive eruptions from the same volcano, or within a single eruption. Some well-known examples of volcanoes that display large variations in eruptive styles between eruptions include Merapi (Indonesia; [Suroño et al., 2012](#)), Soufrière Hills (Montserrat; [Young et al., 1998](#)), and Mt. St. Helens (United States; [Pallister et al., 1992](#)). Examples of how a single volcanic eruption can also rapidly transform from effusive to explosive and vice versa were observed in the 1991 Pinatubo eruption ([Bernard et al., 1996](#); [Pallister et al., 1996](#); [Scaillet and Evans, 1999](#)), the 2009 eruption at Redoubt ([Bull and Buurman, 2013](#)), the 2011 eruption at Puyehue-Cordón Caulle ([Jay et al., 2014](#); [Elissondo et al., 2016](#)). The changes in eruptive style between eruptions are typically abrupt and difficult to anticipate, which makes the mitigation of associated hazards necessary but incredibly challenging.

Changes in eruptive styles can be due to a range of factors. For example, effusive to explosive eruption transition within an eruptive period can be driven by syn-eruptive processes related to water exsolution from the melt and microlite crystallization, which can induce rapid changes in physical properties of the magma that dramatically alter its potential for explosivity in the conduit ([Woods and Koyaguchi, 1994](#); [Melnik and Sparks, 2002](#); [1999](#)). The magma's density, viscosity, and ascent rate change as the magma moves toward the surface and goes through the brittle-ductile transition ([Dingwell et al., 1993](#); [Cashman and Sparks, 2013](#)). The evolution of these parameters is inter-related as a high volatile content in the melt that can produce a buoyant magma, which may accelerate during ascent as long as the volatile bubbles and magma do not decouple ([Corsaro and Pompilio, 2004](#)).

The physical and chemical properties of the magmas before ascent can be primed at their pre-eruptive storage zones. This includes the storage pressure, temperature, crystallinity, melt composition, and dissolved volatile contents. The pre-eruptive volatile content of the melt is particularly important in determining how parameters change, namely, the magma viscosity, buoyancy, and ascent rate ([Giordano et al., 2008](#); [Gonnermann and Manga, 2013](#); [Cassidy et al., 2018](#)). In addition, the presence of an excess volatile phase at pre-eruptive conditions due to second boiling ([Sisson and Bacon, 1999](#)) and volatile fluxing ([Caricchi et al., 2018](#)) has also been shown to be important in driving explosive eruptions ([Scaillet and Evans, 1999](#); [Shinohara, 2008](#); [Longpré et al., 2014](#); [Edmonds and Woods, 2018](#)), although it may have the opposite effect and lead to effusive eruptions ([Popa et al., 2021](#); [2020](#)). Yet it is still unclear whether the build-up of excess volatiles in the magma can influence the style of consecutive eruptions, and how these relate to unrest records.

In this study, we experimentally investigate the crystallization conditions and processes of the explosive-effusive-explosive eruptions of Kelud volcano (Indonesia), as exemplified by the 1990, 2007, and 2014 events. We also report new petrological observations and calculate mineral-melt geothermobarometers that we combine with experimental results to constrain the pre-eruptive storage conditions of the three eruptions. We found that the magmas that fed the 1990, 2007, and 2014 events were essentially stored at similar temperatures, pressures, and water content in the melt. Comparison of the S emissions to the atmosphere by satellite data with those degassed from the melt suggest that the explosivity of the 1990 and 2014 eruptions was driven by the presence of an exsolved excess volatile phase prior to eruption, which was lacking in the 2007 dome eruption. The existence of an exsolved phase at the source likely induced higher buoyancy and faster ascent rates compared to the slower ascent, enhanced degassing, and subsequent re-equilibration of the magma toward the surface that ultimately produced a dome in 2007.

2 Kelud volcano and an overview of the 1990, 2007, and 2014 eruptions

Kelud (Kelut) volcano is an active basaltic-andesite semi-plugged composite strato-cone complex situated in East Java, Indonesia ([Wirakusumah, 1991](#); [Whelley et al., 2015](#)). The volcano hosts a persistent circum-neutral crater lake during repose ([Bernard and Mazot, 2004](#)), and explosive eruptions typically generate syn-eruptive and post-eruptive cold lahars ([Thouret et al., 1998](#)). Kelud typically generates short-lived explosive eruptions that escalate from the onset of unrest to eruption in mere hours ([Lesage and Suroño, 1995](#); [Global Volcanism Program, 2013](#); [Maeno et al., 2019a](#)). Kelud has erupted at least 32 times in the last 100 years ([Global Volcanism Program, 2013](#)), but here we focus on the last three eruptions in 1990, 2007, and 2014.

The 1990 explosive eruption began after ~3 months of unrest followed by quiescence for ~3 weeks ([Bourdier et al., 1997a](#); [1997b](#)). The final escalation toward eruption occurred in hours, giving communities only 1 hour to evacuate their homes ([Global Volcanism Program, 1990a](#)). The explosive eruption in 2014 largely followed a similar pattern in terms of duration of heightened unrest period of the 1990 eruption, although this was condensed into 1 month starting in January 2014. The final escalation toward eruption in 2014 was a steep increase in seismicity of only a few hours ([Hidayati et al., 2019](#)). These 1990 and 2014 events generated eruptive columns as high as 10–17 km ([Bourdier et al., 1997a](#); [Kristiansen et al., 2015](#); [Nakashima et al., 2016](#)) with a VEI of 4 and dense rock equivalent (DRE) volumes of $6.3 \times 10^7 \text{ m}^3$ (1990) and $2.1 \times 10^8 \text{ m}^3$ (2014), respectively ([Maeno et al., 2019a](#)). Moreover, the eruptions were short-lived and volcanic activity and unrest returned to

background levels within days to weeks of the main eruptive phase (Global Volcanism Program, 1990b; Global Volcanism Program, 2014; Global Volcanism Program 1990b).

The lava dome extrusion of November 2007 was preceded by some unrest that started as early as January 2007 (Lubis, 2014), with up to 11 cm of inflation around the summit region detected using ALOS-PALSAR interferometric synthetic aperture radar (InSAR). From July to August 2007, unrest involved intense degassing on the lake floor and an increase in seismicity (Hidayati et al., 2019), and lake temperature rising up (from ~30 to ~75°C), as well as heightened CO₂ emissions from the lake (Global Volcanism Program, 2007; Kunrat, 2009; Caudron et al., 2012). Continuous seismic unrest started around September 2007, involving multiple swarms and low frequency earthquakes (Hidayati et al., 2009). The seismic unrest was further accompanied by inflation from 9th October until 3rd November, when the signal changed to deflation and gave way to slow dome extrusion (Hidayati et al., 2019). The 2007 dome was 200 m high and 400 m wide, with a volume of 3.5×10^7 m³, which is about half the volume of the 1990 eruption (Global Volcanism Program, 2008), but about one order of magnitude smaller than the 2014 event (Maeno et al., 2019a). Despite the diverse monitoring data available, it is still difficult to anticipate eruptions at Kelud, including whether the ensuing eruption will be effusive or explosive (Nakamichi et al., 2017), and this is the main subject of our study.

3 Materials and methods

We conducted petrological analyses of two 2007 dome fragments, previously studied in Humaida (2013), two pumices were sampled following the 2014 eruption (sampled by H. Humaida), and it included the data from the six main-stage pumices from the 1990 eruption studied in Utami et al. (2021). We chose one basaltic andesite pumice from the 1990 eruption studied by Utami et al. (2021) (KELUD1990PL1, or 'PL1') as the starting material for our phase equilibria experiments. The pumice had the same mineral assemblage as other samples, except for the absence of olivine.

3.1 Selection of experimental conditions

We experimentally investigated a range of intensive variables that includes the estimates from mineral-melt geothermobarometers (Utami et al., 2021). We varied the temperature from 950 to 1,060°C, pressure from 100 to 400 MPa, f_{O_2} at the Ni–NiO buffer (NNO) and up to two log units above (NNO +2), and varied a volatile composition in the capsule from pure water to pure CO₂ (see below for more details).

3.2 Preparation of experimental charges

A starting glass was prepared by finely crushing the pumice using a ceramic mortar and pestle and homogenized by fusing the powder at 1,400°C and atmospheric pressure for around 6 h in a standard thermconcept furnace at 1750°C. EPMA analyses of the fused glass confirmed that the glass was homogenous and of the same composition as the whole rock. This glass was crushed again to a fine dry powder with an agate mortar and pestle, which was used as a starting material for all phase equilibrium experiments. About 0.03 g of dry glass was loaded in Au capsules (of size 10–15 mm × 2.5 × 0.2 mm wall thickness) for the 950 and 1,000°C experiments, whereas Au–Pd capsules were used for the 1,060°C experiments.

We varied the fluid composition in the charges (referred to as $X_{H_2O_{in}} = \text{initial } H_2O/[H_2O + CO_2]$ in moles) from 0 to 1 by adding various amounts of deionized water and CO₂ (in the form of silver oxalate) to the dry glass powder, according to the methodology of Scaillet et al. (1995). All the successful runs were fluid saturated. The capsules were arc-welded and weighed before being stored in a 60°C oven to homogenize the fluid content for 6–12 h. After each experiment, the capsule was re-weighed again to check for fluid loss during storage and subsequent experiments. To determine whether the charges were properly sealed, their weight had to be within 0.0005 g of the original value, which is the precision of the analytical balance. We observed that capsules from successfully quenched experiments were shrunk and flattened but had the same weight as before the experiment. Upon opening, the charges ejected gas with an audible pop. In contrast, failed charges appeared bloated and commonly showed a difference in mass (>0.0005 g) between before and after the experiments.

3.3 Experimental equipment

All experiments were conducted at the Institut de Sciences de la Terre Orléans, France using internally heated pressure vessels (IHPV), following the procedure outlined in Scaillet and Evans (1999). Argon was used as a pressurizing medium mixed with different H₂ concentrations at room temperature to establish different f_{O_2} conditions (ranging from NNO to NNO +2), and using a Shaw membrane to establish and maintain the f_{H_2} osmotic equilibrium (Scaillet et al., 1992). A factory calibrated pressure transducer was used to measure and monitor pressure (± 2 MPa), whereas temperature was monitored with unshielded type-S thermocouples, and the temperature of the IHPV "hotspot" was maintained at $T < 10^\circ\text{C}$ and with an uncertainty of $\pm 5^\circ\text{C}$ (Scaillet et al., 1992). Experiment temperatures were increased from room temperature directly up to run temperature in around an hour: each experimental run contained around 4–7 capsules, including one sensor for f_{O_2} (see below). Once the target conditions were achieved, experiments

were run for 18–66 h. Experiments were terminated with a drop-quench device, allowing the sample holder to fall in the cold part of the vessel at the bottom (<50°C), ensuring isobaric quenching and cooling rates of 100°C/s. A fast quench device was set up as part of the experiments (Roux and Lefèvre, 1992). Previous studies (Scaillet and Evans, 1999; Prouteau and Scaillet, 2003; Costa et al., 2004; Andújar et al., 2013) have shown that crystal-melt equilibrium is attained using the same set of protocols. General observations of equilibrium include homogeneous glass composition within the charge, lack of chemical zoning in experimental crystals, and systematic changes in petrologic variables (e.g., crystal content) with experimental variables (temperature and water content). Equilibrium, rather than quench-textures, are characteristic of the run products we report, and we believe they reflect attainment of chemical equilibrium at the desired run conditions.

3.4 Calculation of fO_2 and dissolved water content in experimental charges

The oxygen fugacity (fO_2) was calculated using a sensor capsule containing two water-saturated (10 mg added water), hand-pressed Ni–Pd–NiO powder pellets separated by inert ZrO powder (Taylor et al., 1992). We forgot to add a sensor capsule for one experimental run ($T = 1,060^\circ\text{C}$, $p = 200$ MPa), and thus the final calculated fO_2 for the fluid saturated charge ($XH_2O_{in} = 1.0$) is the average fO_2 of the two closest isobaric runs ($T = 1,060^\circ\text{C}$, $p = 100$ and 400 MPa). For unsaturated charges, we calculated the fO_2 according to the following formula employed by Scaillet and Evans (1999):

$$fO_2^{charge} = fO_2^{sensor} + 2\log_{10} XH_2O_{final\ melt}^{charge},$$

where fO_2 (charge) is the calculated oxygen fugacity of the charge, fO_2 (sensor) is the sensor oxygen fugacity, and the $XH_2O_{final\ melt}^{charge}$ is the proportion of dissolved water content in the melt (see Table 5). We could not calculate fO_2 for dry charges (no water in the melt). Finally, the water content of the experimental glasses was obtained by determining the fluid composition with mass-balance calculations to determine the proportion of fluids put into the charge (XH_2O_{in}) partitioned into the fluid (XH_2O_{fluid}) and melt (XH_2O_{melt}) phases during the experiments. The H_2O solubility model from Shishkina et al. (2010) and the pure CO_2 model from Dixon (1997) were combined to calculate XH_2O_{fluid} and XH_2O_{melt} . From these proportions we calculated the dissolved water content in the melt.

We also compared our dissolved water contents with water contents calculated using the mixed H_2O – CO_2 ‘MagmaSat’ model of Ghiorso and Gualda (2015) using VESICAL (v. 1.0.1; Iacovino et al., 2021). The differences between our initial calculation and MagmaSat model were ≤ 1 wt% (see

Supplementary Material), which use as the nominal error in the water contents we reported. We used the 1σ of this difference as the error in the water content. To maintain consistency in other water contents reported, we calculated the saturation pressures with the same model. To do this, we also used VESICAL (v. 1.0.1; Iacovino et al., 2021) to calculate the saturation pressure with the hybridized models of Shishkina et al. (2010) pure H_2O and Dixon (1997, ‘VolatileCalc’) pure CO_2 model for all three eruptions. This hybridized model simulated the models we used to calculate the water content in the melt. We find that the differences are <300 bars or <30 MPa, which was within error of mineral-melt geobarometers.

3.5 Analytical techniques

Whole-rock analyses of samples, including the pumice starting material, were ground and fused into a lithium tetraborate disk before being analyzed for whole rock major element oxide compositions using X-ray fluorescence (XRF) at the Activation Laboratory in Ancaster, Canada, following the approach outlined in Norrish and Hutton (1969). Mineral proportions were obtained by counting the phenocryst content, using JMicrovision software on plain polarized images of the entire thin section (for the 1990 samples), and using a Pelcon mechanical point counting stage (for the 2007 and 2014 samples). For each sample, we counted between ca. 1,400–1,600 points to ensure statistically significant results with relative errors of <10%. Results from point counting (Table 2) and mineral compositions (Table 3) allowed us to determine the composition of the *calculated matrix* of the 1990, 2007, and 2014 samples (Table 1) by subtracting the mineral compositions weighted with their proportions from the whole rock compositions. Such calculations were necessary to remove the effect of the extensive microlite crystallization for the 2007 dome and to compare with experimental glass. We also used the calculated matrix for geothermobarometric calculations.

We made general observations of experimental charges and identified phases using the scanning electron microscope (SEM) at ISTO-Orléans, France and the Earth Observatory of Singapore. From these images, we determined the crystal content of the experimental charges by thresholding the greyscale of multiple back-scattered electron (BSE) images of a charge map using ImageJ, and we estimated the volumetric area of phases in all charges. With these results, we calculated the mass proportions of the main minerals using standard mineral densities.

Minerals and glass from natural samples and experimental charges were analyzed for their chemical compositions on the JEOL JXA-8530F electron microprobe (EPMA) at the Facility for the Analyses Characterization, Testing, and Simulation (FACTS), Nanyang Technological University, Singapore. Analyses of orthopyroxene, clinopyroxene, olivine, and Fe–Ti

TABLE 1 Representative whole rock and glass compositions for the starting glass, whole rock, clinopyroxene-hosted melt inclusions, and interstitial glass from the 1990, 2007, and 2014.

	Whole rock ^a	Whole rock	Whole rock	Starting dry glass	Calculated matrix ^b	Measured interstitial glass ^a	Calculated matrix ^b	Measured interstitial glass	Calculated matrix ^b	Cpx glass inclusion ^a	Cpx glass inclusion
Eruption year	1990	2007	2014	1990	1990	1990	2007	2014	2014	1990	2014
N	1	1	1	10	1	23	1	5	1	23	5
Normalized wt%											
SiO ₂	54.3	54.9	55.3	55.0 (0.4)	63.0	68.5 (1.4)	72.9	67.1 (0.38)	60.56	69.4 (1.5)	68.5 (0.8)
TiO ₂	0.70	0.64	0.65	0.64 (0.11)	0.34	0.53 (0.07)	0.20	0.61 (0.07)	0.32	0.49 (0.06)	0.64 (0.07)
Al ₂ O ₃	19.00	18.62	18.55	18.97 (0.13)	17.42	15.33 (0.41)	11.91	15.45 (0.22)	18.79	16.09 (0.42)	15.60 (0.25)
FeO*	9.28	9.15	8.95	8.92 (0.56)	5.18	4.12 (0.30)	2.75	4.57 (0.16)	4.85	2.77 (0.77)	4.05 (0.18)
MnO	0.20	0.20	0.20	0.19 (0.03)	0.17	0.15 (0.03)	0.11	0.17 (0.05)	0.15	0.12 (0.03)	0.16 (0.06)
MgO	3.67	3.71	3.60	3.81 (0.06)	2.28	1.13 (0.14)	0.69	1.37 (0.06)	2.09	0.49 (0.18)	0.99 (0.07)
CaO	9.08	9.04	8.97	8.74 (0.04)	6.77	3.87 (0.38)	5.11	4.45 (0.11)	8.65	2.94 (0.26)	3.55 (0.29)
Na ₂ O	2.91	2.90	2.98	2.93 (0.07)	3.13	4.48 (0.20)	3.78	4.35 (0.18)	3.33	4.77 (0.41)	4.37 (0.12)
K ₂ O	0.69	0.68	0.69	0.68 (0.03)	1.35	1.59 (0.12)	2.11	1.57 (0.10)	1.05	1.78 (0.17)	1.63 (0.07)
P ₂ O ₅	0.16	0.13	0.14	0.13 (0.02)	0.33	0.21 (0.03)	0.43	0.25 (0.03)	0.20	0.25 (0.06)	0.24 (0.03)
Total ^c	99.7	101.1	101.0	100.4 (1.0)	100.0	98.9 (1.1)	100.0	99.0 (0.4)	100.0	94.9 (1.3)	93.6 (0.7)
Na ₂ O+K ₂ O	3.60	3.58	3.67	3.62 (0.08)	4.48	6.07 (0.26)	5.88	5.91 (0.21)	4.38	6.08 (0.50)	5.73 (0.27)
SO ₂ (ppm)	n.a.	n.a.	n.a.	n.a.	n.a.	46–110	n.a.	b.d.	n.a.	316–904	278–565
Cl (wt%)	n.a.	n.a.	n.a.	0.03 (0.01)	n.a.	0.12 (0.02)	n.a.	0.13 (0.01)	n.a.	0.19 (0.01)	0.16 (0.02)

^aAverage values of compositions from [Utami et al. \(2021\)](#).

^bCalculated matrix is determined from whole rock composition minus mineral chemistry (in major element oxide) weighted by mass proportion (see *Methodology* section). ^cIndividual major element oxide compositions are normalized in wt%, but the original total is presented.

Note. n. a. = not analyzed. b.d.l. = below detection limit.

oxides were performed on the EPMA in spot mode with 15 kV accelerating voltage, beam size of 1 μm , and 20 nA beam current. Amphibole and plagioclase were analyzed in spot mode with 15 kV accelerating voltage, beam size of 1 μm , and 10 nA current. Glass was analyzed in spot mode with 6 kV, beam size of 10 μm , and 5 nA current. The same conditions and procedures were used to observe and analyze the glasses and minerals of the 2007 and 2014 rocks. For clinopyroxene-hosted glass inclusions, we corrected for post-entrapment crystallization of the melt inclusion walls (Buchholz et al., 2013). The relative errors for glasses are 0.4–0.8% for SiO_2 , Al_2O_3 , and CaO; 1–3% for MgO, FeO, Na_2O , K_2O ; and 9–41% MnO, TiO_2 , P_2O_5 , and Cl. For pyroxenes, the relative errors are 0.2–1.0% for SiO_2 , Al_2O_3 , CaO, MgO, FeO; 1–30% for Na_2O and K_2O ; and 2–55% MnO, TiO_2 , and Cr_2O_3 . Relative errors for Fe–Ti oxide analyses are 0.3–0.6% for FeO, 0.5–7.5% for TiO_2 , 0.5–1.8% for MgO. For olivine analyses are 0.2–0.5% SiO_2 , MgO, FeO; and 0.8–18% Al_2O_3 , CaO, MnO. The relative error for amphibole analysis is 0.3–0.8% for SiO_2 , Al_2O_3 , CaO, FeO, MgO; 4.2–4.4% MnO, TiO_2 ; and 11–30% for Na_2O and K_2O .

The mineral end-members were calculated using their molar compositions as in Utami et al. (2021), and with formulations according to Deer et al. (1992). Pyroxenes are characterized with the Mg # ($\text{Mg \#} = 100 \times \text{Mg}/[\text{Mg} + \text{Fe}^*]$ in mol, where Fe^* is total iron as Fe^{2+}). We further characterize pyroxenes using their wollastonite ($\text{Wo} = 100 \times \text{Ca}/[\text{Ca} + \text{Mg} + \text{Fe}^*]$), ferrosilite ($\text{Fs} = 100 \times \text{Fe}/[\text{Ca} + \text{Mg} + \text{Fe}^*]$), and enstatite ($\text{En} = 100 \times \text{Mg}/[\text{Ca} + \text{Mg} + \text{Fe}^*]$) endmembers. Plagioclase end member compositions were classified using their molar compositions for anorthite ($\text{An} = 100 \times \text{Ca}/[\text{Ca} + \text{Na} + \text{K}]$), albite ($\text{Ab} = 100 \times \text{Na}/[\text{Ca} + \text{Na} + \text{K}]$), and orthoclase ($\text{Or} = 100 \times \text{K}/[\text{Ca} + \text{Na} + \text{K}]$). Olivine is characterized using the forsterite content ($\text{Fo} = 100 \times \text{Mg}/[\text{Mg} + \text{Fe}^*]$), whereas amphibole is classified according to the compositional end-members outlined in Leake et al. (1997), as determined by Ridolfi et al. (2010). Glass compositions were characterized using their normalized to 100% anhydrous major element oxides and total alkali-silica (TAS) composition. It was difficult to obtain good quantitative analyses of plagioclase crystals in experimental charges as they are typically small and may contain Fe–Ti oxide inclusions. To be able to report approximate An contents of plagioclase, we have filtered for analyses with $\text{FeO}^* < 1 \text{ wt\%}$ and $\text{TiO}_2 < 0.1 \text{ wt\%}$, and subtracted the composition of magnetite from the electron microprobe analyses to match these constraints. We report these recalculated compositions to fit the structural formulas labeled ‘-N.’

3.6 Remote sensing of SO_2 emissions

To evaluate sulfur dioxide (SO_2) emissions from Kelud during the 2007 effusive eruption, we used ultraviolet (UV)

satellite data from the Ozone Monitoring Instrument (OMI) on NASA’s Aura satellite. Aura/OMI was launched in 2004 and has a spatial resolution at nadir of $13 \times 24 \text{ km}$ and high sensitivity to atmospheric SO_2 , permitting detection of small plumes emitted by weak or passive volcanic degassing (Carn et al., 2016). OMI measurements since 2004 have provided a long-term record of passive and eruptive volcanic SO_2 emissions that continues to the present (Carn et al., 2017, 2016; Carn, 2022). Column amounts of SO_2 are derived from the UV OMI measurements using a low-noise principal component analysis (PCA) retrieval algorithm (Li et al., 2017); the SO_2 column amounts measured in a volcanic plume are integrated to obtain SO_2 mass. The OMI SO_2 retrievals are altitude-dependent, and here we assume a lower tropospheric (TRL) SO_2 plume altitude ($\sim 3 \text{ km}$ above sea level) to approximate the expected volcanic plume altitudes at Kelud (summit elevation $\sim 2 \text{ km}$). The results presented here are the first detailed analysis of OMI SO_2 measurements for the 2007 Kelud eruption.

We note that Kelud was not identified as a major source of persistent volcanic SO_2 emissions in the 2005–2015 period covered by the global inventory of Carn et al. (2017), indicating that passive SO_2 emissions from the volcano are generally absent or below OMI detection limits (~ 20 – 80 tons/day). However, Semeru, Bromo, Raung and Kawah Ijen volcanoes, located to the east of Kelud, are all persistently active (Carn et al., 2017), and their SO_2 plumes are often advected west over the Kelud region, which can impact the detection of Kelud’s SO_2 emissions in an easterly wind regime. Frequent cloud cover and convection over the higher elevations of East Java can also hamper the detection of volcanic SO_2 emissions by OMI.

4 Results

4.1 Petrological observations and geothermobarometry of the 1990–2007–2014 magmas

We document petrological observations and calculate geothermobarometric estimates from the deposits of the 1990, 2007, and 2014 eruptions. Whole rock major elements vary over a small range across eruptions, and samples are classified as basaltic andesite (Table 1). The calculated matrix compositions, the measured interstitial glasses, and clinopyroxene-hosted melt inclusions are of a similar dacitic composition (see Utami et al., 2021). The three eruptions have deposits with different phenocryst ($> 100 \mu\text{m}$) content: 31–47 wt% in the 1990 pumices; 70–72 wt% for the 2007 dome; and 29–35 wt% in 2014 pumices (Table 2). The mineral assemblage for all three eruptions includes phenocrysts of plagioclase (Plag), clinopyroxene (Cpx), orthopyroxene (Opx), and magnetite (Mag).

TABLE 2 Mineral assemblage and phenocryst content of samples from 1990, 2007, and 2014 eruptions.

Sample label	90–23 ^a	PL1 ^a	2007A	2007B	14-PUMI-1	14-PUMI-2
Eruption	1990	1990	2007	2007	2014	2014
Phase ^b	wt%	wt%	wt%	wt%	wt%	wt%
Glm ^c	52.8	69.1	27.8	30.2	70.5	65.1
Plag	37.6	14.1	48.2	47.7	21.2	19.9
Cpx	3.3	6.6	4.6	3.9	1.2	2.1
Opx	3.9	5.4	10.6	12.0	3.0	7.5
Mag	2.4	4.8	8.5	6.2	3.6	4.7
Amph		<0.1	0.3		0.5	
Ol		<0.1				0.7
Apa ^d	<0.1	<0.1	<0.1	<0.1	<0.1	<0.1
Total	100.0	100.0	100.0	100.0	100.0	100.0
Phenocryst content ^e	47.3	30.9	71.9	69.8	29.0	34.2

^aSamples PL1 and 90–23 here are the same as ‘1990-PL1’ and ‘90–23’ that were reported in [Utami et al. \(2021\)](#).

^bOpx = orthopyroxene; Cpx = clinopyroxene; Plag = plagioclase; Mag = magnetite; Ol = olivine; Amph = amphibole; Apa = apatite.

^cGlm means the sample’s matrix.

^dApatite was identified as an accessory mineral.

^ePhenocryst size is defined as grains larger than 100 μm .

Accessory minerals include apatite (Apa), which is found in all three eruptions. Quartz (Qz)-rich enclaves occur in the 1990 late-stage pumice; cristobalite (Crs) is found as vesicle infill in the 2007 dome samples (see [Supplementary Figure S3](#)). Ilmenite (Ilm) is present as rims around Mag in the 1990 late-stage pumice and as exsolution lamellae in Mag in the 2007 deposits (see [Supplementary Material](#)). The 1990 and 2014 pumices also host partially reacted amphibole (Amph), and we have also identified pseudomorphs of Amph megacrysts and symplectites after Ol breakdown in the 2007 dome, meaning that both Amph and Ol may have also been stable in the 2007 magma (see [Supplementary Figure S3](#)). We also found partially reacted olivine (Ol) microphenocrysts (<100 μm) in the 2014 pumice. The compositions of the main minerals of the three eruptions are also broadly similar, with the histograms of compositional mineral indicators (e.g., Mg Number) typically overlap for the three eruptions ([Figures 1A–C](#); [Table 3](#)) and are also similar to those of previous studies from the same eruptions (e.g., [Jeffery et al., 2013](#); [Cassidy et al., 2019](#); [2016](#)).

We made geothermobarometric estimates under the 1990–2014 magma storage conditions from mineral and whole rock/calculated matrix compositions ([Table 4](#)). For this we use core-whole rock and rim-calculated matrix pairs (see also [Utami et al., 2021](#) for the 1990 eruption). The pyroxene-liquid or two pyroxene equilibria formulations of [Putirka \(2008\)](#) give temperatures that range from about 1,030°C for the crystal cores, to about 975°C (down to 950°C) for the crystal rims. Moreover, the mineral and glass compositions of the three eruptions give pre-eruptive temperatures that are within about $\pm 30^\circ\text{C}$ ([Table 4](#)). These temperature estimates also

overlap with those obtained from amphibole-melt equilibria at about 960°C for the 1990 and 2014 eruptions. Pressure estimates we obtained come from the amphibole-melt geobarometer formulation of [Putirka \(2016\)](#), where pressures range from 450 MPa up to 700 MPa for the 1990 and 2014 eruptions, respectively.

The dissolved water content in the 1990 and 2014 magmas are calculated using the plagioclase-melt hygrometer of [Waters and Lange \(2015\)](#), with temperatures calculated using Opx-melt geothermometers of mineral core/whole rock and rim/calculated matrix pairs. For the 2007 dome, we use the core/whole rock pair for the Opx-melt temperatures and adjacent Opx–Cpx pairs for the two-pyroxene temperatures. Water contents range from 3.1 to 4.7 wt% ([Table 4](#)), which are consistent with previous estimates in [Utami et al. \(2021\)](#). These water contents in the melt correspond to H₂O–CO₂ saturation pressures of ~170–220 MPa using the combined model of [Shishkina et al. \(2010\)](#) and [Dixon \(1997\)](#). These pressures are also similar to the range of pressures obtained in [Utami et al. \(2021\)](#). The water content in the melt estimated for the 2007 samples using plagioclase rim and core, and the calculated matrix glass is about 3 wt% water, which is slightly lower than those of the 1990 and 2014 eruptions.

4.2 General observations from the experimental results

Successful experimental charges range from complete glass to almost fully crystallized. Glass-rich charges are devoid of vesicles ([Figure 2](#)). Most charges ([Figures 2B–H](#)) have a porphyritic

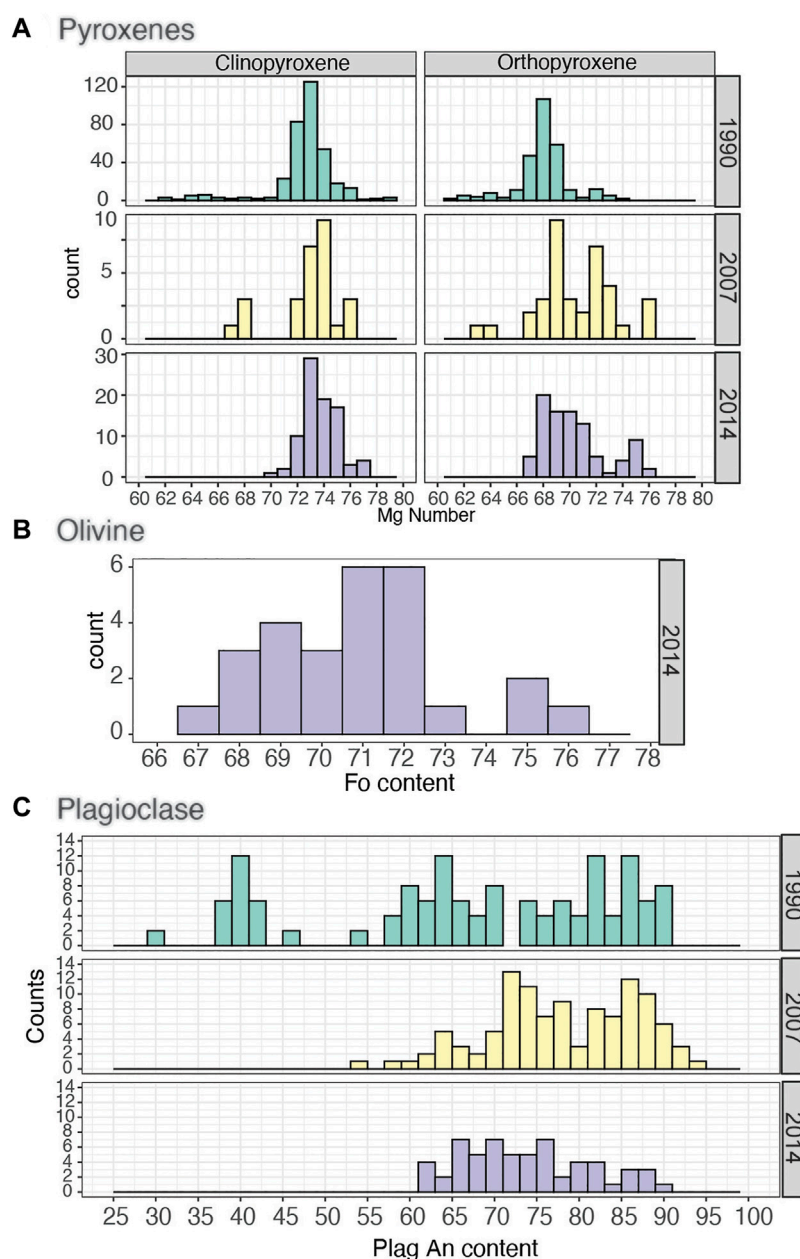


FIGURE 1

Histograms of representative mineral compositions from the 1990–2014 eruptions (A) pyroxenes, (B) olivine, and (C) plagioclase. Plagioclase composition from the 2014 eruption comes from a combination of this study and Cassidy et al. (2016) and those of the 1990 from Utami et al. (2021).

texture, with subhedral to euhedral crystals set in interstitial glass with vesicles. Crystals may vary in size from phenocrysts ($>100\ \mu\text{m}$) to microlites ($<10\ \mu\text{m}$). Typically, Opx and Ol are subhedral to euhedral, commonly with Mag and Plag inclusions ($>100\ \mu\text{m}$) (Figure 2C). Some charges have clusters of Fe–Ti oxides microlites, as well as Fe–Ti oxides distributed throughout the charge (Figure 2D). Despite the large range in crystal sizes, minerals, and glass appear to be unzoned, according to BSE

images, which is likely indicative of compositional equilibrium. Due to the small size of many crystals, it was very challenging to obtain a good quantitative chemical analysis, and thus we relied on mineral identification using EDS spectra obtained in SEM or electron probe. We obtained glass compositions from glass-rich experimental charges or for those where glass “pools” larger than about $10\ \mu\text{m}$, and we found that they are homogeneous in composition (Figures 2A–D). For charges with low water

TABLE 3 Summary of representative mineral compositions from the 1990–2014 eruptions.

Mineral	Plag	Plag	Plag	Plag	Mineral	Amph ^c	Amph
Eruption year	1990	2007	2014	1990	2007	2014	2014
Rock type/stage	Main-stage pumice	Dome	Pumice	Main-stage pumice	Dome	Pumice	
Texture	Cores, glomerocryst	Cores, glomerocryst	Cores, glomerocryst	Cores, glomerocryst	Glomerocryst	Cores, glomerocryst	
N	8	16	26	20	7	27	27
wt%							
SiO ₂	51.6 (0.7)	51.8 (0.4)	51.2 (0.6)	52.7 (0.2)	52.9 (0.1)	52.7 (0.5)	SiO ₂ 36.9 (0.4)
TiO ₂	0.48 (0.30)	0.33 (0.04)	0.36 (0.07)	0.28 (0.12)	0.16 (0.01)	0.19 (0.04)	TiO ₂ 0.02 (0.02)
Al ₂ O ₃	1.78 (0.62)	1.71 (0.18)	2.00 (0.44)	1.24 (0.34)	0.91 (0.17)	1.09 (0.36)	Al ₂ O ₃ b.d.
FeO*	9.24 (0.58)	9.54 (0.16)	9.48 (0.26)	18.53 (1.18)	19.2 (0.2)	18.44 (1.38)	FeO* 25.9 (1.6)
MnO	0.50 (0.09)	0.52 (0.03)	0.49 (0.05)	0.87 (0.18)	0.90 (0.04)	0.84 (0.11)	MnO 0.65 (0.09)
MgO	14.47 (0.09)	14.30 (0.23)	14.40 (0.22)	23.5 (0.5)	22.84 (0.07)	23.71 (0.90)	MgO 35.1 (1.4)
CaO	21.1 (0.4)	20.8 (0.3)	20.8 (0.3)	1.71 (0.43)	1.44 (0.08)	1.59 (0.22)	CaO 0.18 (0.05)
Na ₂ O	0.27 (0.02)	0.29 (0.02)	0.28 (0.02)	0.02 (0.01)	0.02 (0.01)	0.01 (0.01)	P ₂ O ₅ 0.04 (0.04)
Total	99.4 (0.2)	99.3 (0.4)	99.0 (0.3)	98.9 (0.3)	98.4 (0.1)	98.6 (0.4)	Total 98.8 (0.4)
Pyroxene end-members ^a							
Wo	43.6 (0.8)	43.2 (0.6)	43.1 (0.6)	3.50 (0.87)	2.99 (0.16)	3.24 (0.44)	Fo content ^b 70.7 (2.1)
En	41.6 (0.3)	41.3 (0.5)	41.6 (0.5)	66.9 (1.2)	65.9 (0.3)	67.4 (2.0)	
Fs	14.88 (0.91)	15.46 (0.31)	15.34 (0.42)	29.6 (2.0)	31.1 (0.2)	29.4 (2.4)	
Mg Number	73.7 (1.3)	72.8 (0.5)	73.0 (0.6)	69.3 (1.8)	67.9 (0.2)	69.6 (2.4)	

Mineral	Plag	Plag	Plag	Plag	Mineral	Amph ^c	Amph ^c	Amph
Eruption year	1990	2007	2014	2014	Eruption year	1990	1990	2014
rock type/stage	Main-stage pumice	Dome	Pumice	Pumice	Rock type/stage			
Texture	Microlite/rim	Rim	Core	Rim	Texture			
n of new spots	11	12	4	2	N	13	4	4
SiO ₂	50.9 (1.3)	50.6 (1.3)	45.3 (1.4)	51.0 (0.1)	SiO ₂	41.3 (0.2)	42.5 (0.5)	43.7 (3.1)
Al ₂ O ₃	30.2 (0.6)	30.4 (0.9)	33.6 (0.3)	29.3 (0.1)	TiO ₂	1.47 (0.10)	1.54 (0.14)	1.60 (0.60)
FeO*	0.45 (0.16)	0.62 (0.06)	0.53 (0.05)	0.67 (0.01)	Al ₂ O ₃	15.14 (0.32)	13.92 (1.01)	11.37 (3.99)
MgO	0.07 (0.02)	0.06 (0.02)	0.01 (0.01)	0.08 (0.01)	FeO*	11.25 (0.28)	11.29 (0.19)	11.33 (2.05)
CaO	13.58 (0.45)	13.48 (0.88)	17.93 (0.90)	13.42 (0.05)	MnO	0.15 (0.01)	0.17 (0.02)	0.19 (0.13)
Na ₂ O	4.06 (0.23)	3.62 (0.50)	1.31 (0.18)	3.86 (0.08)	MgO	13.84 (0.25)	14.21 (0.11)	15.15 (1.0)
K ₂ O	0.09 (0.02)	0.09 (0.03)	n.a.	n.a.	CaO	12.06 (0.16)	11.71 (0.07)	11.14 (1.63)
Total	99.4 (1.0)	98.9 (0.6)	98.7 (0.8)	98.35 (0.01)	Na ₂ O	2.25 (0.08)	2.23 (0.02)	1.77 (0.67)
Plag end-member ^d				Cl	K ₂ O	0.31 (0.02)	0.29 (0.02)	n.a.
An	64.4 (1.8)	67.0 (4.5)	89.2 (0.9)	65.8 (0.5)	F	0.01 (0.01)	0.01 (0.01)	n.a.
Ab	35.1 (1.7)	32.5 (4.4)	10.8 (0.9)	34.2 (0.5)	Total	0.08 (0.07)	0.15 (0.12)	n.a.
Or	0.4 (0.2)	0.50 (0.15)	n.a.	n.a.	Amph end-member ^e	97.9 (0.5)	98.0 (0.2)	96.2 (0.8)
					Mg-Hst		Ts-Prg	Ts-Prg

^aPyroxene end-members: wollastonite, $Wo = 100 \times Ca/[Mg + Fe^* + Ca]$; enstatite, $En = 100 \times Mg/[Mg + Fe^* + Ca]$; ferrosilite, $Fs = 100 \times Fe^*/[Mg + Fe^* + Ca]$; $Mg \# = 100 \times Mg/[Mg + Fe^*]$.
^bOlivine Fo content, $Fo = 100 \times Mg/[Mg + Fe^*]$.
^cAmphibole composition from [Utami et al. \(2021\)](#).
^dPlagioclase end-members: anorthite, $An = 100 \times Ca/[Ca + Na + K]$; albite, $Ab = 100 \times Na/[Ca + Na + K]$; orthoclase, $Or = 100 \times K/[Na + Ca + K]$.
^eAmphibole end-members according to [Leake et al. \(1997\)](#), as calculated in [Ridolfi et al. \(2010\)](#). Mg-Hst = magnesio-hastingsite; Ts-Prg = Tschermakite-Pargasite.
 Notes. n. a. = not analyzed, and b.d. = below detection limit. FeO^+ or Fe^* = total Fe as Fe^{2+} . Glom = glomerocryst. See [Table 2](#) for meaning of mineral abbreviations.

TABLE 4 New storage condition estimates from mineral-melt geothermobarometers, hygrometers, and H₂O–CO₂ saturation models for the 1990, 2007, and 2014 mineral populations.

Year of eruption	1990				2007				2014			
	Core		Rim		core ^a		Core		Rim			
Texture	n	T (°C)	n	T (°C)	n	T (°C)	n	T (°C)	n	T (°C)		
Opx-melt ^b	75	1,023 (19)	37	976 (17)	2	1,032 (2)	15	1,039 (15)	1	974		
Cpx-melt ^b	122	1,043 (13)	23	1,045 (34)	5	1,029 (3)	18	1,028 (6)				
Two-pyroxene ^{b,c}	67	1,023 (40)	67	1,030 (43)	2	980 (9)			7	948 (8)		
Ol-melt ^b							8	1,018 (5)				
Year of eruption	1990				2007				2014			
Hygrometer	Texture	n	H ₂ O _{melt} (wt%)	P _{sat} (MPa) ^d	Texture	n	H ₂ O _{melt} (wt%)	P _{sat} (MPa) ^d	Texture	n	H ₂ O _{melt} (wt%)	P _{sat} (MPa) ^d
Plag-melt ^e	Core	27	4.7 (0.2)	246 (9)	Core	82	4.4 (0.1)	230 (7)	Core	2	4.5 (0.1)	232 (2)
	Rim	19	3.5 (0.1)	170 (2)	Rim	28	3.1 (0.2)	156 (10)	Rim	2	3.5 (0.1)	173 (1)
	Microlite	5	3.5 (0.1)	169 (3)								
Year of eruption	1990			2007			2014					
Geothermobarometer	n	T (°C)	P _{store} (MPa)	n	T (°C)	P _{store} (MPa)	n	T (°C)	P _{store} (MPa)			
Amph-melt ^f	20	960 (10)	450 (80)	Not analyzed			8	940 (80)	700 (90)			

^afor 2007 dome, Opx-, and Cpx-liquid geothermometer calculations used whole rock/core mineral compositions. Plag-melt hygrometer calculations used whole rock/Opx-melt temperatures for cores, and calculated interstitial glasses/two-pyroxene temperatures for rims.
^bOl-melt geothermometer (Eq. 21; SEE = ± 36°C [5].); Opx-melt geothermometer (Eq. 28a; SEE = ± 39°C); Cpx-melt geothermometer (Eq. 33; SEE = ± 42°C); and two-pyroxene geothermometer (Eq. 37; SEE = ± 60°C) from [Putirka \(2008\)](#).
^cQUILF, two-pyroxene geothermometer ([Andersen et al., 1993](#)); SEE = ± 37°C, assuming a constant pressure of 100 MPa ([Utami et al., 2021](#)).
^dSaturation P is calculated using VESICAL ([Iacovino et al., 2021](#)) with hybrid of pure H₂O model ([Shishkina et al., 2010](#)) + pure CO₂ model ([Dixon, 1997](#)) + water content from Plag-melt hygrometer ([Waters and Lange, 2015](#)). CO₂ content taken from [Cassidy et al. \(2016\)](#) (Max: 336 ppm).
^eDissolved water contents were calculated using the Plag-melt hygrometer by [Waters and Lange \(2015\)](#) (SEE ±0.35 wt%) with plag compositions from [Utami et al. \(2021\)](#) and this study. Temperatures are from Opx-melt and two-pyroxene geothermometers from [Putirka \(2008\)](#).
^fAmph-melt geothermobarometer (Eq. 7a SEE = ± 30°C) from [Putirka \(2016\)](#) with Al/Si equilibrium test described in [Li et al. \(2021\)](#) (K_d (Al/Si)= 0.96 ± 0.4).
 Notes. See [Table 2](#) for meaning of mineral abbreviations. Parameters in italics are average calculated values from [Utami et al. \(2021\)](#) and this study. The Standard Error of Estimate for mineral-melt geothermobarometers and hygrometers is abbreviated to SEE, numbers in brackets refer to the standard deviation away from the calculated mean, or 1σ.

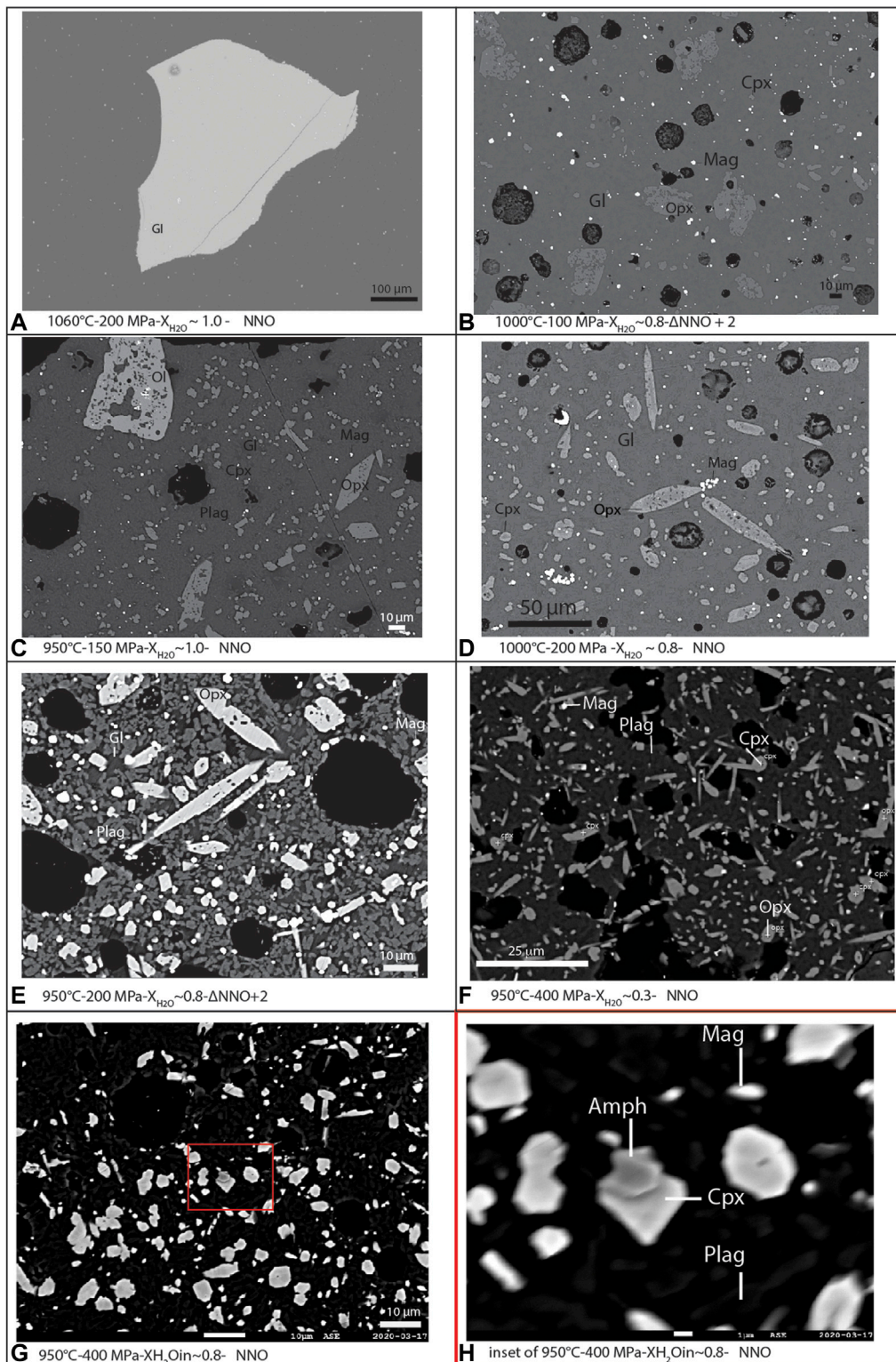


FIGURE 2

Annotated BSE images of selected representative experimental charges in order of increasing crystallinity. (A) 1,060°C-200 MPa-NNO. (B) 1,000°C-100 MPa- Δ NNO + 2. (C) 950°C-150 MPa-NNO. (D) 1,000°C-200 MPa-NNO. (E) 950°C-200 MPa- Δ NNO + 2. (F) 950°C-400 MPa-NNO. (G) 950°C-400 MPa-NNO. (H) Inset of charge in (G) Labeled with abbreviated mineral names (Gl = glass, Plag = plagioclase, Cpx = clinopyroxene, Opx = orthopyroxene, Mag = magnetite, and Amph = amphibole).

TABLE 5 Summary of experimental conditions, calculated melt volatile contents, and run products and their phase proportions.

Charge ID	log (fO ₂) d (bar)	ΔNNO ^e	XH ₂ O _{in} ^f	Calculated melt volatile content ^a			Phase proportions ^{b,c} (wt%)								
				XH ₂ O _{melt}	H ₂ O _{melt} (wt%)	CO ₂ - melt (wt. ppm)	Opx	Cpx	Plag	Mag	Ilm	Ol	Amph	Gl	
<i>T = 1,000°C, p = 100 MPa, t = 66 h</i>															
SUPL1-1	-9.5	0.8	1.00	1.0	3.5	0	6.0	2.8	30	1.1			3.4		56
SUPL1-2	-9.8	0.6	0.80	0.7	3.0	162	12.4	8.1	30	2.1					48
SUPL1-3	-10.0	0.3	0.66	0.6	2.5	267	13.2	8.7	34	2.7					42
SUPL1-4	-10.1	0.2	0.56	0.5	2.3	312	14.9	8.3	43	2.3					32
<i>T = 1,000°C, p = 150 MPa, t = 19 h</i>															
SUPL1-5	-8.5	1.8	1.00	1.0	4.4	0	18.0	25	2.0						55
SUPL1-6	-8.7	1.6	0.82	0.8	3.8	250	3.7	2.3	23	0.5			4.3		66
SUPL1-7	-9.0	1.4	0.67	0.6	3.2	414	13.1	7.6	30	1.8					48
SUPL1-8	-9.0	1.3	0.63	0.6	3.1	444	13.4	12.1	35	1.8					38
SUPL1-9	-9.5	0.9	0.41	0.3	2.3	633	13.4	5.3	56	3.7					22
SUPL1-10	n.a.		0.00	0.0	0.0	888	24		58			0.7			17.9
<i>T = 1,000°C, p = 200 MPa, t = 22 h</i>															
SUPL1-11	-9.4	0.9	0.84	0.7	3.0	421	7.6	4.1	26	0.9					62
SUPL1-12	-9.6	0.8	0.75	0.6	3.9	573	5.1	6.8	29	1.0					58
SUPL1-13	-9.9	0.4	0.55	0.4	3.1	835	11.2	8.2	36	1.2					44
SUPL1-14	-10.7	-0.4	0.30	0.2	1.8	1,090	14.6	15.3	36	0.6					34
SUPL1-15	n.a.	n.a.	0.00	0.0	0.0	1,263	25		53			0.6			21
<i>T = 1,000°C, p = 400 MPa, t = 23 h</i>															
SUPL1-16	-9.5	0.8	0.85	0.7	6.5	1,681	13.9	1.8	5.6	0.3				<0.01	78
SUPL1-17	-10.4	0.0	0.54	0.3	3.8	2,977	16.5	12.0	22	0.3					50
SUPL1-18	-11.4	-1.0	0.27	0.1	1.9	3,438	16.0	12.0	28	0.8					43
SUPL1-19	n.a.	n.a.	0.00	0.0	0.0	3,638	25		38			0.4			37
<i>T = 950°C, p = 150 MPa, t = 66 h</i>															
SUPL1-20	-10.0	1.1	1.00	1.0	4.3	0	7.1	1.2	19.3	3.5			5.1		64
SUPL1-21	-10.2	0.9	0.84	0.8	3.7	245	14.4	3.6	29	4.3					48
SUPL1-22	-10.3	0.8	0.75	0.7	3.5	327	16.8	7.6	28	0.6					47
SUPL1-23	-10.8	0.3	0.49	0.4	2.5	582	14.0	10.8	34	0.8					41
SUPL1-24	-11.0	0.1	0.39	0.3	2.2	647	13.5	11.0	42	0.6					32
SUPL1-25	n.a.	n.a.	0.00	0.0	0.0	890	36		52			0.5			12.0
<i>T = 950°C, p = 200 MPa, t = 49 h</i>															
SUPL1-26	-10.7	0.4	1.00	1.0	5.1	0	19.9	13.2	29	3.0					35
SUPL1-27	-10.9	0.2	0.86	0.8	4.6	291	19.0	7.6	38	4.3				<0.01	31
SUPL1-28	-11.1	0.0	0.68	0.6	3.8	588	17.7	21	32	0.9					29
SUPL1-29	-11.4	-0.3	0.54	0.4	3.2	797	12.8	15.4	44	1.6					26
<i>T = 950°C, p = 400 MPa, t = 67 h</i>															
SUPL1-30	-9.8	1.3	1.00	1.0	8.1	0	17.9	8.4	10.7	3.2					60
SUPL1-31	-10.3	0.8	0.78	0.6	5.8	2066	14.3	3.7	16.0	3.0				<0.01	63
SUPL1-32	-10.6	0.6	0.71	0.4	4.9	2,526	11.2	3.9	29	3.2					52
SUPL1-33	-11.0	0.1	0.50	0.3	4.3	3,029	11.0	2.9	35	3.2					48
SUPL1-34	-11.5	-0.4	0.35	0.1	2.6	3,322	12.9	10.2	31	2.7					44
SUPL1-35	n.a.	n.a.	0.00	0.0	0.0	3,685	30		39			0.4			30

(Continued on following page)

TABLE 5 (Continued) Summary of experimental conditions, calculated melt volatile contents, and run products and their phase proportions.

Charge ID	log (fO ₂) d (bar)	ΔNNO ^e	XH ₂ O _{in} ^f	Calculated melt volatile content ^a			Phase proportions ^{b,c} (wt%)						
				XH ₂ O _{melt}	H ₂ O _{melt} (wt%)	CO ₂ - melt (wt. ppm)	Opx	Cpx	Plag	Mag	Ilm	Ol	Amph
<i>T = 1,060°C, p = 100 MPa, t = 18 h</i>													
SUPL1-36	-8.1	1.4	1.00	1.0	3.6	0			29	1.9			69
SUPL1-37	-8.4	1.1	0.78	0.7	3.0	168			57	2.4		<0.1	41
SUPL1-38	-8.5	1.0	0.73	0.6	2.8	220			46	3.6		0.9	49
SUPL1-39	-8.6	0.9	0.67	0.6	2.6	251	4.9	3.1	44	0.4			48
SUPL1-40	-9.2	0.2	0.37	0.3	1.7	424	9.5	7.7	44	3.7			35
SUPL1-41	n.a.	n.a.	0.00	0.0	0.0	563	23	0.8	38		12.6		26
<i>T = 1,060°C, p = 200 MPa, t = 94 h</i>													
SUPL1-42	-8.4	1.1	1.00	1.0	5.3	0			0.8				99
SUPL1-43	-8.9	0.5	0.72	0.5	3.6	696	16.6	2.1	16.9	2.1			62
SUPL1-44	-9.3	0.1	0.53	0.3	2.8	914	12.9	7.9	28	0.9			50
SUPL1-45	-10.3	-0.8	0.27	0.1	1.4	1,153	20	1.3	38	2.0			39
SUPL1-46	n.a.	n.a.	0.00	0.0	0.0	1,260	21		43	0.9			35
<i>T = 1,060°C, p = 400 MPa, t = 49 h</i>													
SUPL1-47	-8.6	0.9	1.00	1.0	8.6	0							100
SUPL1-48	-10.1	-0.7	0.59	0.2	3.0	3,206	2.7	1.8	13.8	0.2			81
SUPL1-49	-11.6	-2.1	0.22	0.0	1.1	3,543	9.1	6.4	22	1.7			61
<i>T = 1,000°C, p = 100 MPa, t = 77 h</i>													
SUPL1-50	-8.4	1.9	1.00	1.0	3.5	0	5.8	5.6	26	3.2		0.9	59
SUPL1-51	-8.6	1.7	0.83	0.8	3.0	143	11.0	2.5	29	2.8			55
SUPL1-52	-8.7	1.6	0.77	0.7	2.9	178	11.8	4.3	31	2.8			51
SUPL1-53	-9.0	1.3	0.57	0.5	2.3	311	13.7	4.1	38	3.1			41
SUPL1-54	-9.4	0.9	0.42	0.3	1.8	399	16.0	11.1	33	0.4			39
SUPL1-55	n.a.	n.a.	0.00	0.0	0.0	564	24		45		2.4		29
<i>T = 1,000°C, p = 200 MPa, t = 19 h</i>													
SUPL1-56	-8.5	1.8	1.00	1.0	5.2	0	14.3	3.1	15.7	0.6			66
SUPL1-57	-8.7	1.6	0.85	0.8	4.5	355	2.0	1.5	20	1.0		4.0	71
SUPL1-58	-8.9	1.4	0.73	0.6	3.9	575	6.4	4.7	21	3.3		5.9	58
SUPL1-59	-9.1	1.2	0.59	0.5	3.5	726	13.2	6.3	28	1.6			51
SUPL1-60	-10.0	0.3	0.29	0.2	1.9	1,086	15.5	13.0	28	3.0			41
SUPL1-61	n.a.	n.a.	0.00	0.0	0.0	1,263	23		39		9.4		29
<i>T = 950°C, p = 200 MPa, t = 71 h</i>													
SUPL1-62	-9.3	1.8	1.00	1.0	5.1	0	15.3	18.0	19.9	1.0			46
SUPL1-63	-9.5	1.7	0.86	0.8	4.5	303	16.7	5.2	31	3.7			43
SUPL1-64	-10.0	1.1	0.54	0.4	3.1	804	15.0	11.1	34	3.1			36
SUPL1-65	-10.9	0.2	0.28	0.2	1.7	1,104	25	22.2	21	0.5			30
SUPL1-66	n.a.	n.a.	0.00	0.0	0.0	1,266	43		41		0.6		15.4

^aWater and CO₂ content in the melt were calculated from mass balance and the combined solubility models of Shishkina et al. (2010) for pure H₂O and Dixon (1997) for pure CO₂.

^bPhase proportions were calculated using grayscale thresholding of BSE, charge maps using ImageJ software and then converted to phase proportions.

^cSee Table 2 for meaning of abbreviations, with the addition of Gl that we refer to glasses only. For charges where only CO₂ was added, we could not calculate the log (fO₂).

^dlog (fO₂) determined using water saturated Ni–Pd alloy capsules, calculated using the formulation by Pownceby and O'Neill (1994). For undersaturated charges, we calculated the fO₂ using the formula outlined in Section 3.4.

^eΔNNO, log (fO₂) - log (fO₂) at Ni–NiO, buffer.

^fXH₂O_{in} = H₂O/(H₂O + CO₂) loaded in capsules in moles.

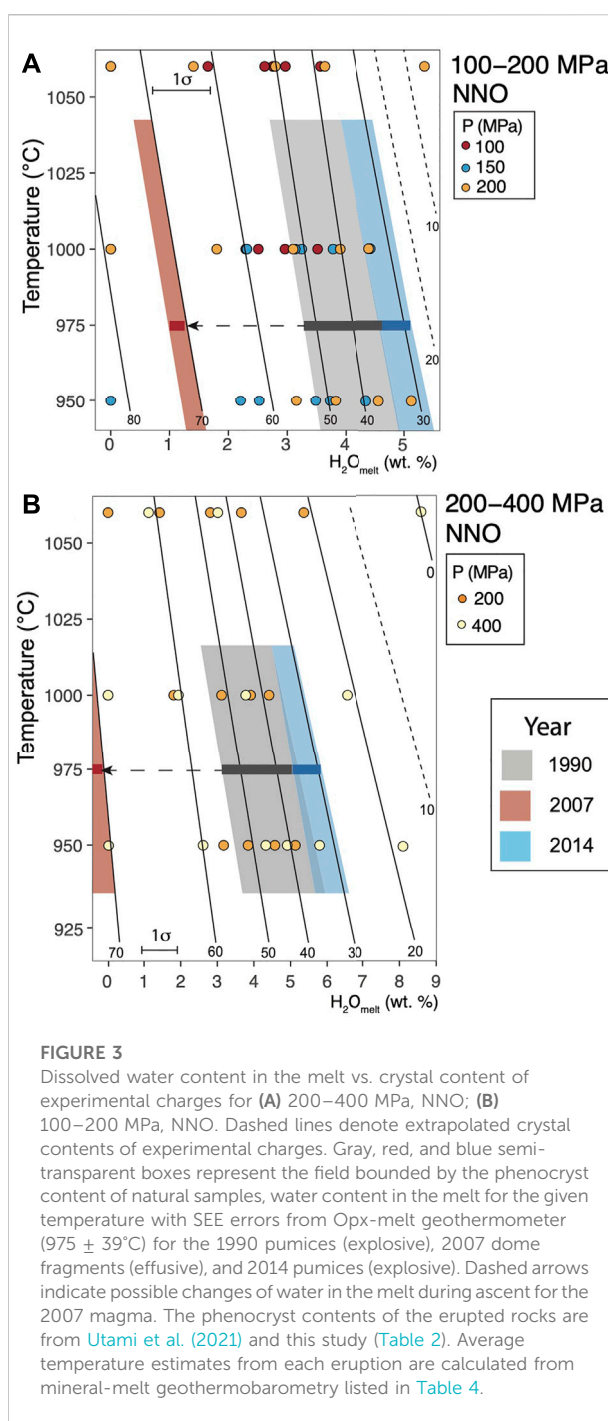
contents, phases are often very small to analyze. For charges that failed, that is, where the fluid escaped the capsule during the experiment, we consistently observe a very high crystal content and a quench texture, with abundant microlites of Opx and Plag, and rare Ilm and glass; these were not used further.

4.3 Phase relation, crystallinities, and mineral assemblages

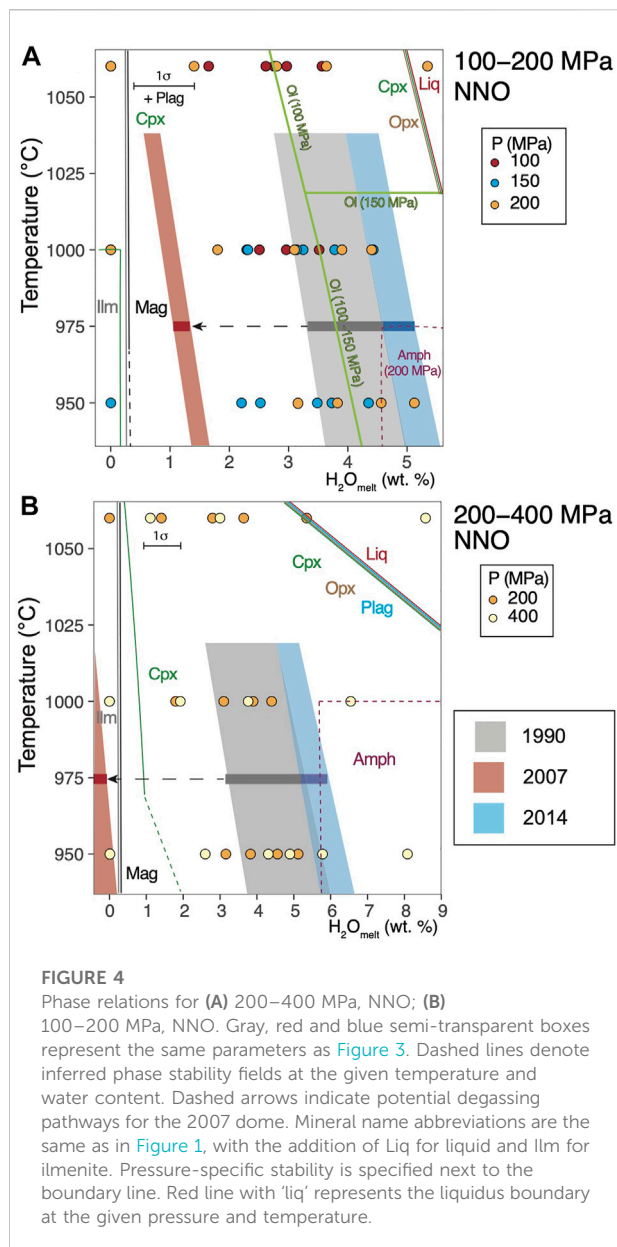
The complete experimental phase assemblage of all charges includes Opx, Plag, Cpx, Mag, Ilm, Amph, Ol, and glass (Figures 2A–H). We did not identify experimental apatite, but it may be present. The crystal content from experimental charges varies from virtually none to about 88 wt% (Table 5). The crystal content generally increases as both temperature and water content decreases and as fO_2 increases. We produced liquidus or near-liquidus experiments with <1 wt% of crystals, at 1,060°C (Figure 2B), and in charges at water saturated conditions (about 5–9 wt% H_2O in the melt), 200–400 MPa, and fO_2 of NNO (Figures 4A–C). These conditions match the model liquidus temperature calculated from rhyolite-MELTS in Utami et al. (2021). At 100 and 200 MPa and 1,000°C, the crystal content varies between about 68 and 44 wt% for 2–4 wt% water in the melt. Increasing the temperature to 1,060°C decreases the crystal content to 52 to 31 wt% at 3–4 wt% water in the melt, but it increases up to 74 wt% for <2 wt% in the melt. Similar changes in the crystal content with temperature and water content in the melt for different experimental pressures (see Supplementary Material). Increasing fO_2 from NNO to NNO +2 results in an increase in the proportion of magnetite toward slightly higher crystal contents.

The relationship between crystallinity, temperature, and water content in the melt can be used to obtain first-order constraints on the ‘pre-eruptive conditions’ (Figure 3). By ‘pre-eruptive conditions’ we mean those that best reproduce the natural phenocryst content, the mineral assemblage, and when possible, the phase compositions. They apply to the conditions before the magma started to move toward the surface and erupted. We have neither directly investigated the syn-eruptive processes, such as microlite density or size, nor the vesicle characteristics, as was conducted in decompression experiments (Martel, 2012). Such definition of pre-eruptive storage conditions is relatively straightforward to apply to the explosive eruptions of 1990 and 2014, which quickly moved toward the surface. However, it is more ambiguous for the 2007 dome, which ascended more slowly and re-equilibrated to lower volatile contents, and contains a higher amount of phenocrysts. We attempt to clarify these differences in the following paragraphs.

Using a temperature of magma storage of $975 \pm 39^\circ\text{C}$ for the three eruptions, as suggested by geothermobarometric data of all eruptions (Table 4), we find that the melt of the 1990 and



2014 magmas could contain about 4–6 wt% water at 150–200 MPa (Figures 3, 4). At 100 MPa and 400 MPa, this range corresponds to 3–4 wt% and 5–7 wt% water in the melt, respectively (Supplementary Figures S7, S8). The considerably higher phenocryst content of the 2007 dome would imply significantly lower water content in the melt (~1 wt%). However, as we have discussed in the geothermobarometry results section earlier, we believe this does not reflect the



storage conditions before the magma started to move toward the surface. In addition to the same temperature, the plagioclase-matrix equilibria suggest similar water contents in the melt for all eruptions. Thus, we propose that the trend reflects re-equilibration and maturation during slow ascent; in essence, we consider this an initial ascent phase of that eruption, which allowed for degassing and consequent crystallization.

We find that experimental Opx and Plag are present at all conditions below the liquidus, and the Cpx stability field is somewhat smaller (Figures 4A–C, Supplementary Figure S4). Although we suspect amphibole was stable in our charges by comparison with the results of other phase equilibrium studies with similar bulk compositions (Pichavant et al., 2002; Prouteau

and Scaillet, 2003; Erdmann et al., 2016), we were not able to confidently identify it with EDS spectra or quantitative electron microprobe analysis owing to the high crystallinity of the charges and its small crystal size. To circumvent this problem, we applied principal component analysis to electron microprobe analyses of mineral compositions using the R package 'FactoMineR' (Lé et al., 2008), and we successfully identified experimental amphibole at 950–1,000°C and 200–400 MPa, with 4.5–6 wt% water in the melt (Figures 4A,B), which overlaps with our pressure estimates from natural amphiboles from the 1990 and 2014 eruptions. We identified experimental Ol with 3–4 wt% water in the melt at NNO and <150 MPa (Figure 4B). At NNO +2, Ol stability extends to higher pressures and water content (at 200 MPa, 1,000°C, and about 4–6 wt% water in the melt; Figure 4C). The stability of Fe–Ti oxides is also controlled by the dissolved water content and fO_2 . Ilmenite is stable at lower dissolved water contents than Mag, whereas with increasing fO_2 makes magnetite more stable at low water contents.

4.4 Mineral and glass compositions

We strived to quantitatively analyze as many phases in as many charges as possible. However, we were only able to obtain a limited number of quantitative compositions, given the small sizes of many phases as described in the methods. This makes it difficult to directly make a close match between the natural phase compositions to the experimental ones, although we found some overlapping compositions at similar P–T–water under the melt conditions that was suggested by the crystallinity and phase assemblage relations (Figures 3, 4). Data tables for experimental mineral compositions are found in the Supplementary Tables S3–S7.

4.4.1 Glass

Experimental glass compositions vary with water content, temperature, and pressure (Figures 5A–L), with compositions evolving from basaltic andesite to dacite as temperature decrease from 1,060 to 950°C (Supplementary Table S3). The most evolved glass composition that we are able to analyze is dacitic with 68 wt% SiO₂ at 200 MPa, 1,060°C, NNO, 1 wt% water in the melt, and with 50–54 wt% crystals in the charge (Figure 5A). The glass we analyzed from the rest of the charges ranges from basaltic andesite to andesite. For the same temperature, pressure, and fO_2 , the major element oxides such as SiO₂ and K₂O increase as the water content in the melt decreases, indicating the melt is becoming more evolved (Figures 5A–C, J–L). Conversely, oxides such as Al₂O₃ and CaO decrease with decreasing water content. Changing the fO_2 from NNO to NNO +2 does not significantly affect the SiO₂ content of the melt for the same pressure, temperature, and dissolved water content. The FeO* (3–9 wt%), MgO (1.5–7 wt%), and TiO₂ (0.7–1.7 wt%) of experimental glasses (see Supplementary Figure S4) are controlled by

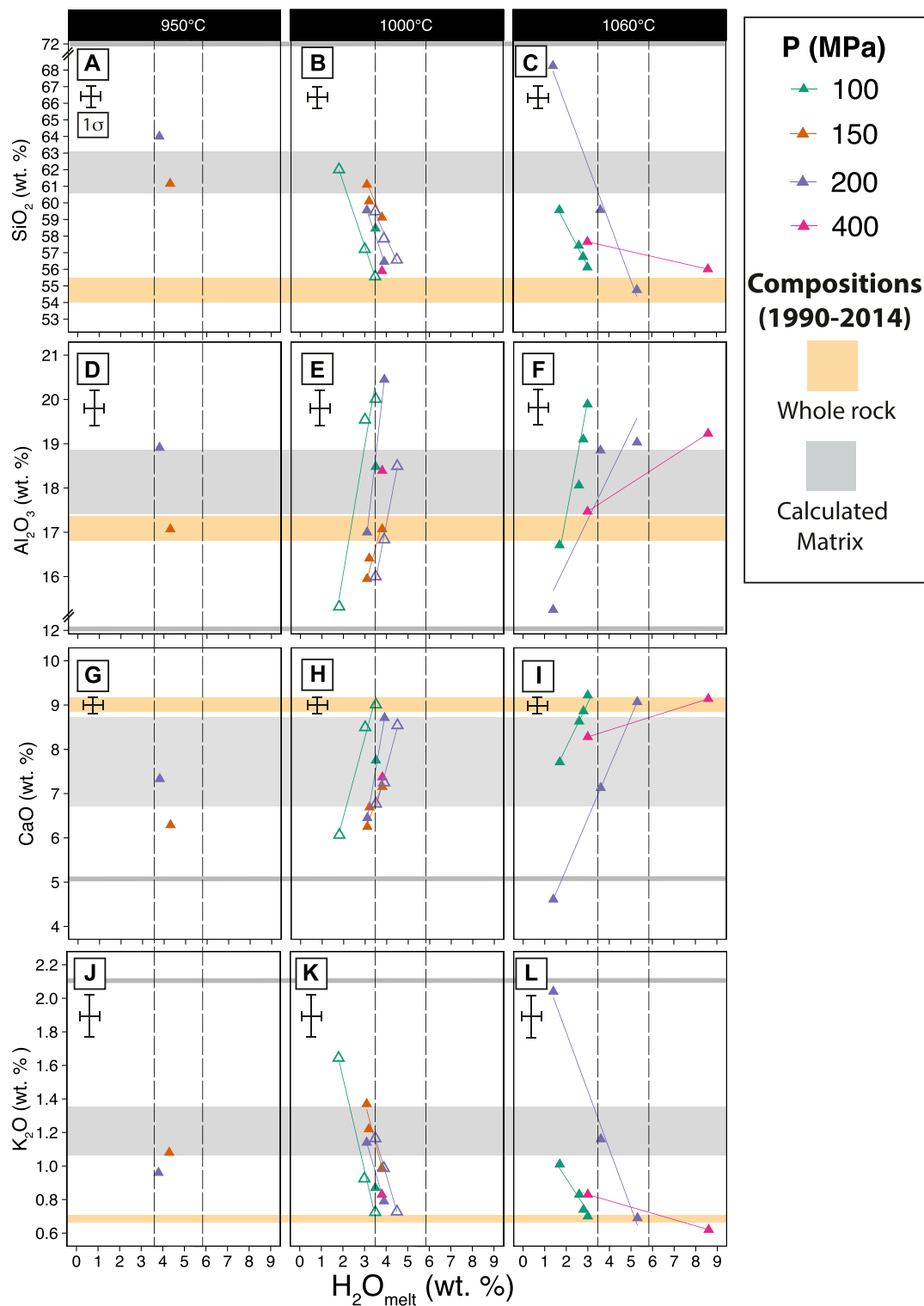


FIGURE 5

Major element oxide compositions of experimental glasses (in wt%) vs. dissolved water content in the melt according to three different temperatures SiO₂ (A) 950°C, (B) 1,000°C, (C) 1,060°C; Al₂O₃ (D) 950°C; (E) 1,000°C, (F) 1,060°C; CaO (G) 950°C; (H) 1,000°C; (I) 1,060°C; K₂O (J) 950°C, (K) 1,000°C, (L) 1,060°C. Yellow horizontal band denotes the range of whole rock compositions. The thick gray band is the composition of calculated matrix for the explosive eruptions (1990, 2014); the thin gray band is the calculated matrix of the 2007 dome (Table 1). The calculated matrix compositions for the 1990, 2007, and 2014 eruptions were estimated by mass balance calculations (Albarede, 1995) (see Methodology section). Vertical dashed lines are water content in the melt inferred from crystallinity and phase assemblage (Figures 3, 4). Filled symbols represent experiments at NNO; open lined symbols represent experiments at NNO +2.

crystallization of ferromagnesian minerals such as pyroxenes and magnetite. The limited number of natural and experimental glasses that we are able to analyze means we do not have a direct match to the natural compositions. Yet the calculated matrix and the experimental glasses overlap at around 950–1,000°C, 150–200 MPa, 4–4.5 wt% water in the melt, and fO_2 of NNO to NNO +2. The general lack of agreement between the calculated matrix and experimental glasses in some major element oxides (e.g., FeO and K_2O) could be due to the effect of syn-eruptive crystallization of Plag and oxide microlites in natural rocks. We also observe microlites in one 1990 pumice and the 2007 dome, which may explain why the natural rocks have a higher SiO_2 content than the experimental glasses.

4.4.2 Plagioclase

It is difficult to obtain “pure” analyses of experimental plagioclase due to its elongated shape (e.g., very thin in one direction) and the presence of mineral inclusions such as oxides and/or pyroxenes, so we report the recalculated analyses after subtraction of the effect of mineral inclusions (see *Methodology* section). We first filtered the experimental Plag analyses for their FeO^* and TiO_2 contents to remove Mag inclusions. Yet the MgO content remains higher than expected for a plagioclase (~1 wt%). We thus suspect that there may be some analyses that are mixtures of Plag and Opx, which we have not attempted to correct further. However, this should not affect the relative Ca–Na–K concentrations and thus determination of the stoichiometric Plag end-members. Experimental plagioclase ranges in composition from about An_{59} to An_{65} (Supplementary Table S4; Figure 6A), and varies according to the water content in the melt and to a lesser extent, by temperature. For the same T, P, and fO_2 , we find that the water content negatively correlates with An content. We have neither been able to analyze experimental Plag for near liquidus charges nor from those with very high crystal content. Some of the experimental Plag compositions overlap with natural Plag microlites and rims from the 1990–2014 eruptions as described in Utami et al. (2021) and in this study with An_{65} (Figure 6A; Supplementary Table S1). Phenocryst rims and microlites (An content from 65 to 68) overlap with experimental Plag that crystallized at 200 MPa, 1,000°C, and 4 wt% water in the melt and at NNO.

No experimental Plag composition that we analyzed have An content >65. However, we find that Plag cores and some oscillatory growth zones from all three eruptions with An content of >71 in this study by Utami et al. (2021) and Cassidy et al. (2016) (see Figure 1 and Supplementary Figure S3). To check whether it is possible to produce Plag with An content of >71 as observed in the 2014 cores (Table 2), we modeled the evolution of the Plag chemistry with rhyolite-MELTS v.1.2.0 using the mixed H_2O – CO_2 model by Ghiorso and Gualda (2015). We used the isobaric crystallization model and the composition of the starting material, with the addition of

4 wt% water and 336 ppm CO_2 in the melt from Cassidy et al. (2016), and fO_2 buffered at NNO. We found that Plag with An content of 70–86 can be produced through isobaric crystallization from 933 to 1,063°C, which is somewhat lower than the highest plagioclase An core compositions at 88–90 (Table 3).

4.4.3 Orthopyroxene

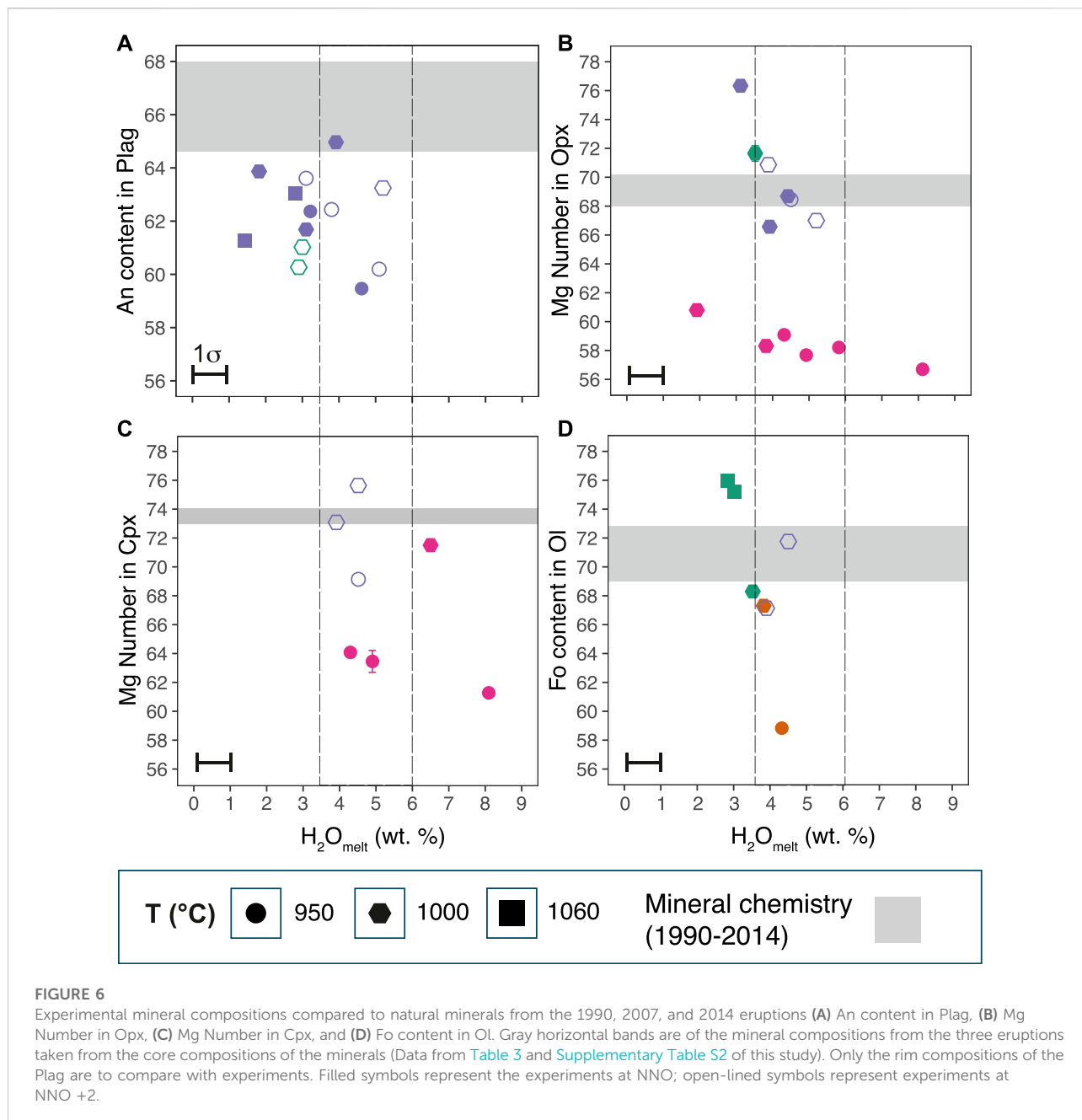
Experimental Opx composition mainly varies with temperature and water content in the melt (Mg Number: 57–71; Figure 6B, Supplementary Table S5). The Wo component of some of the experimental Opx is high (Wo_{6-10}), and is thus classified as pigeonite according to Deer et al. (1992). For the same pressure and fO_2 (e.g., 400 MPa, NNO), a temperature increase from 950 to 1,000°C results in a corresponding increase in the Mg Number of about 56–61; a decrease in the water content in the melt also results in an increase in the Mg Number. A strong influence of water content in the Opx-melt Mg Number partitioning was reported in previous experimental studies (Waters and Lange, 2017). The 1990–2014 Opx cores and glomerocrysts range from Mg Number 66 to 76 (average of 66). This Mg Number range overlaps with experimental orthopyroxene compositions at 1,000°C, 200 MPa, and 4–4.5 wt% water in the melt and NNO to NNO +2 for all eruptions. We have not identified pigeonite in the natural samples.

4.4.4 Clinopyroxene

Experimental Cpx is present in most charges (Mg Number: 61–76, $Wo_{34-41}En_{39-46}Fs_{15-26}$) (Figure 6C, Supplementary Table S5). The Mg Number of experimental Cpx increases from 61 to 76, with increasing temperature and decreasing water content in the melt. There appears to be some effect of pressure, temperature, and water content on the Cpx composition. At 950°C, the experimental Cpx at 200 MPa have higher Mg Number (69–76) than at 400 MPa (61–64); one exception is one Cpx with Mg Number of 72 at 1,000°C, 400 MPa, NNO, and 6 wt% water. The Mg Number increases as water content decreases for isobaric charges at 950°C and 400 MPa. As we could not obtain good quantitative analysis of Cpx for all charges, we have no clear indication of the effect of fO_2 on clinopyroxene composition. The 1990, 2007, and 2014 clinopyroxene cores and glomerocrysts compositions (Mg Number 70–76, average ~74) somewhat overlaps with experimental clinopyroxene at 1,000°C, 200 MPa, ~4 wt% in the melt, and NNO +2.

4.4.5 Olivine

Experimental Ol (Fo content: 59–76) is present in charges at 950–1,000°C, $p = 100$ –150 MPa at NNO, and 1,000°C, 200 MPa, at NNO +2 (Figure 6D, Supplementary Table S6). The Fo content increases strongly with temperature for a water content of 3–5 wt%. There is no discernible systematic change in Fo with increasing fO_2 from NNO to NNO +2. We can only compare



the experimental Ol compositions to Ol from the 2014 eruption because the Ol from the 1990 and 2007 eruptions have completely reacted to symplectites. The Ol population from the 2014 eruption ranges in the Fo content from 67 to 73. The 2014 eruption Ol overlaps with experimental Ol at 200 MPa, 1,000°C, NNO +2, and 4.5 wt% water.

4.4.6 Amphibole

It was particularly difficult to confidently identify Amph in our experimental charges, and we were only able to obtain good quantitative analysis of one experimental Amph

(magnesian-hornblende; Mg Number = 69; Supplementary Table S6) in the charge at 950°C, 400 MPa, and 6 wt% dissolved water in the melt (Figures 2G,H). We also identified additional Amph crystals in other charges using principal component analyses of mineral compositions obtained with EPMA analysis (Supplementary Figure S2). Geothermobarometry results from the natural Amph of the 1990 and 2014 eruptions agree with the experimental Amph stability field we have found (Figure 4). We reconstructed the composition melt from natural Amph from 1990 to 2014 using the Al/Si values, and the methodology of Li et al. (2021) to

compare the equilibrium SiO₂ content of the parental melt of Amph with that of our glasses. We found that the Amph from 1990 is in equilibrium with 53–60 wt% SiO₂ in the melt, which is close to the SiO₂ content of the starting material glass. The Amph from 2014 is in equilibrium with more silica-rich melt of 68–70 wt% SiO₂, which overlaps with the interstitial glasses. This shows that a range of amphibole composition are stable in the Kelud system. However, it is unclear if the difference between the 1990 and 2014 Amph represents a real difference under magmatic crystallization conditions or is an artifact of the sampling and the limited number of Amph compositions we have. We note that there are many examples of fully reacted Amph crystals in erupted products from the three eruptions. For the 2007 dome, this could be to the progressively shallowing of the magma (see the following discussion section); for the 1990 and 2014 eruptions it suggests that the magmas were stored at conditions straddling the boundary of the Amph stability field.

4.4.7 Fe–Ti oxides

Magnetite and less common ilmenite were produced in the experimental charges depending on the water content in the melt. Experimental magnetite ($X_{\text{usp}} = 0.24\text{--}0.60$) is present in almost all water-saturated charges (Supplementary Table S7). Ilmenite occurs in water poor charges. Although we have identified ilmenite in charges with EDS analyses, we were not able to quantitatively determine their compositions.

4.5 SO₂ emissions of 2007 dome extrusion

Kelud emitted around 150 kT and 200–300 kT SO₂ for the 1990 and 2014 eruptions, respectively (Carn, 2022). In 1990, ~150 kT SO₂ was measured on 11 February, around 1 day after the onset of the main Kelud eruption on 10 February. The measured SO₂ emission is therefore a minimum amount. Similarly, most of the SO₂ emissions from the 2014 eruption (~200 kT) was injected during the main phase of the eruption and detected by satellites 12 h after the eruption, meaning the actual emissions could be higher (up to ~300 kT). Thus, we used the total SO₂ emissions for the 1990 eruption (~150 kT) and a range of emissions for the 2014 eruption (~200–300 kT) to calculate the excess SO₂ from each eruption (Table 6).

We analyzed Aura/OMI SO₂ measurements from July 2007 through May 2008, covering the few months prior to the 2007 dome extrusion at Kelud and the approximate duration of lava dome growth. Volcanic SO₂ emissions clearly attributable to Kelud were only apparent on a few days during this period, although, as noted earlier, SO₂ emissions from other active volcanoes in East Java are frequently advected over the Kelud region and may have obscured any weaker emissions from Kelud. However, significant SO₂ emissions from Kelud would still have been detectable.

No significant SO₂ emissions from Kelud were detected in July–October 2007, when Crater Lake temperatures and CO₂ fluxes were elevated (Global Volcanism Program, 2007; Kunrat, 2009; Caudron et al., 2012). It is likely that any SO₂ emissions in this period would have been scrubbed by Kelud's hydrothermal system or Crater Lake. A drifting SO₂ cloud (containing ~100 tons SO₂) was first observed west of Kelud on 2 November 2007, a few days before the new lava dome was first directly observed in the crater (Global Volcanism Program, 2008). This SO₂ cannot be unequivocally attributed to Kelud but could represent emissions associated with the initial dome eruption. A clear SO₂ plume (~200 tons SO₂) was observed south-west of Kelud on November 5, the day after fresh lava dome extrusion was confirmed (Global Volcanism Program, 2008). Further SO₂ emissions from Kelud were detected on November 7 (~140 tons SO₂) and November 25 (~200 tons SO₂). These SO₂ observations were made when a favorable wind direction and/or reduced activity at other East Javan volcanoes allowed us to attribute the detected SO₂ emissions to Kelud with some confidence. After 25 November 2007, no further significant SO₂ emissions from Kelud were detected by OMI during the November 2007–May 2008 dome extrusion phase.

Total observed volcanic SO₂ emissions from Kelud during the 2007 dome extrusion thus amount to ~600–700 tons. However, due to frequent cloud cover and generally weak emissions this likely represents a minimum amount. The coincidence of elevated SO₂ emissions and the beginning of subaerial lava dome effusion in early November 2007 is consistent with other observations of effusive eruptions, which typically show a 'waxing–waning' trend in SO₂ emissions, with peak gas fluxes close to the eruption onset. Using the emissions for the 2007 dome and SO₂ concentrations from Plag-hosted melt inclusions (Jeffery et al., 2013), we calculated the excess SO₂ for the 2007 dome eruption (Table 6).

5 Discussion

5.1 Geothermobarometry and experimental constraints on magma storage conditions of sub-Plinian eruptions and dome extrusions

Combining the geothermobarometric and experimental results, we found that the initial pre-eruptive magma crystallization conditions that match the phenocryst content (Figure 3), natural mineral assemblage (Figure 4), and some of the mineral compositions for the three eruptions (Figure 5) are at $975 \pm 39^\circ\text{C}$, $175 \pm 25\text{ MPa}$, with about 4–6 wt% water in the melt and a $f\text{O}_2$ of NNO. These conditions correspond to about 7 km of storage below the crater if we use a crustal density of $2,640\text{ kg m}^{-3}$. However, geothermobarometry indicates that amphibole which could also be derived from deeper parts are

TABLE 6 Mass balance calculation of SO₂ exsolved from the melt and measured by satellite.

Year of eruption	1990	2007	2014	
Eruption style	Explosive	Lava dome	Explosive	
VEI	4	2	4	
Erupted volume (DRE) ^a	0.13	0.035	0.14–0.28	km ³
Rock density	2,352–2,402	2,500	2,404	kg/m ³
Mass of magma	306–312	88	337–673	Mt
Conc. of SO ₂ in melt inclusion	471–800	256–368 ^b	296–596	ppm
Conc. of SO ₂ in interstitial glass	47–230	300–352 ^b	62–236 ^c	ppm
Glass proportion ^d	0.5–0.7	0.3	0.7	
SO ₂ degassed from the melt	20–164	0–1.7	24–260	kt
Atmospheric SO ₂ ^e	150	0.6–0.7	200–300	kt
Excess SO ₂	0 to 130	0 to 0.7	0 to 276	kt

^aErupted volume for all eruptions are taken from [Maeno et al. \(2019a\)](#), [Maeno et al. \(2019b\)](#).

^bConcentrations of SO₂ in melt inclusion and interstitial glass from the 2007 dome were taken from [Jeffery et al. \(2013\)](#), recalculated from S to SO₂, in ppm.

^cSO₂ concentrations of interstitial glasses from the 2014 eruption pumices are below the detection limit. Instead, the interstitial glass concentrations of ashes from the 2014 eruption were used.

^dData to calculate glass proportions are taken from [Table 2](#). For the 2007 dome, the glass proportion is calculated glass before microlite crystallization.

^eTotal SO₂ emissions for 1990 is from [Carn \(2022\)](#). The 2007 dome emissions are from 5 to 7 November 2007 (this study). Emissions for 2014 eruption is from [Zhu et al. \(2020\)](#) and [Carn \(2022\)](#).

that the 1990 and 2014 amphibole record deep pressures of 450–700 MPa ([Table 4](#)), and many crystals are reacted ([Utami et al., 2021](#); this study). Moreover, the reaction textures in olivine suggest that the magma storage could have straddled the stability fields of amphibole and olivine.

A key difference between the 1990 and 2014 eruptions and that of the 2007 dome is the much higher phenocryst content of the latter ([Table 2](#)). This could be due to crystal accumulation in the dome, but the whole-rock major and trace element compositions of the three eruptions are similar, including incompatible trace elements such as Zr (this study; [Jeffery et al., 2013](#)), meaning that the observed difference in the crystal content is due to *in situ* crystallization. According to experimental results, the lava dome's higher phenocryst content ([Table 2](#); [Figure 3](#)) can be reproduced with ~1 wt% water in the melt for a temperature of about 975°C. Thus, we propose that although the storage conditions for the 2007 magma were similar to that of the 1990 and 2014 magmas before it started moving to the surface, the lower apparent water content is likely the result of slow transport toward the surface that in turn led to water loss and cooling. The slower ascent observed in 2007 resulted in the re-equilibration of phenocryst proportions and compositions to shallower depths.

[Cassidy et al. \(2019\)](#) performed partial melting experiments using samples from the 2014 eruption. They explored a smaller range of P-T and water conditions than we report, and they used a crushed rock as starting material and thus 'partial equilibrium' experiments (for discussion about full vs. partial equilibrium experiments, see [Pichavant et al., 2007](#)). Given the different

experimental approaches, it is not straightforward to directly compare our results to those of [Cassidy et al. \(2019\)](#). Some notable differences are that our experiments crystallized amphibole and olivine (and we also find them in the natural rock), which are absent in [Cassidy et al. \(2019\)](#), but this is likely because we investigated a wider range of experimental parameters. Our inferred crystallization temperatures are similar to those of [Cassidy et al. \(2019\)](#) for all the eruptions, but we find higher pressures and water contents in the melt.

5.2 The importance of excess volatiles in modulating eruption style

The explosive → effusive → explosive eruption sequence shown by the 1990–2007–2014 events is one of the most interesting aspects of Kelud volcano. The contrasting eruptive style is particularly intriguing because we have shown that the "initial" (i.e., before ascent) conditions of temperature, pressure, and water content in the melt are broadly the same for the three events. Other factors that could be responsible for the differences in eruptive style are the conduit dynamics, where parameters such as the magma flow rate and overpressure work together to determine whether the magma will erupt explosively or effusively ([Woods and Koyaguchi, 1994](#); [Mastin, 2002](#); [Campagnola et al., 2016](#)). Syn-eruptive processes at the conduit level certainly played a key role in the eruption style at Kelud, but several observations point toward the importance of other parameters, especially the possible presence of a pre-eruptive volatile phase.

Our mass balance calculations and those of [Utami et al. \(2021\)](#) for the SO₂ budget of the 1990 and 2014 eruptions indicate the presence of an exsolved volatile phase at pre-eruptive conditions, with up to 130 kT SO₂ for the 1990 eruption and 276 kT SO₂ for the 2014 eruption ([Table 6](#)). In contrast, the calculated amount of the exsolved volatile fluid phase for the 2007 dome eruption is virtually negligible. Pre-eruptive excess fluid can be developed *via* progressive magma crystallization and volatile buildup to supersaturation ([Tait et al., 1989](#); [Tramontano et al., 2017](#); [Arzilli et al., 2019](#); [Cassidy et al., 2019](#)), and/or with fluid fluxing from a deep-seated basaltic magma reservoir ([Giuffrida et al., 2017](#); [Caricchi et al., 2018](#)), or limestone assimilation ([Deegan et al., 2016, 2010](#); [Jeffery et al., 2013](#)). Although we can only calculate the amount of SO₂, the fluid phase would have also included other volatiles including water and CO₂. The presence of an exsolved fluid phase under pre-eruptive conditions means the magma buoyancy is greatly increased, as fluids can expand from the moment the magma starts its ascent, lithostatic pressure decreases ([Gonnermann and Manga, 2013](#)).

A critical aspect to the role of exsolved volatiles in the explosivity of the eruption is whether they separate from the melt during transport, and thus increase the magma permeability. [Popa et al. \(2021\)](#) proposed a model where effusive eruptions can be driven by magmas with an exsolved volatile phase under pre-eruptive conditions and a higher water content in the melt (and somewhat hotter due to mafic intrusion) than explosive events. The lower viscosity of the melt combined with the higher bubble content at the starting conditions would facilitate fluid escape through the magma column due to higher permeability, thus decreasing the explosivity. Although this may be responsible for the contrasting eruptive styles at the Nisyros–Yali volcanic system ([Popa et al., 2021; 2020](#)), at Kelud we did not find the magma that produced the dome in 2007 had a lower viscosity than the explosive events ([Utami, 2021](#)). There was also no initial explosive event recorded before the dome extrusion itself ([Global Volcanism Program, 2008](#)). Rather, we propose that the exsolved volatile phase that was likely related to the 2007 magma was passively released during the repose between 1990 and 2007, which was punctuated by at least two significant unrest events involving gas release (see below).

The accumulation of an excess fluid also requires the plumbing system to be a plugged or semi-plugged system during repose ([Whelley et al., 2015](#)), or with the mass flux of exsolved fluids production being larger than that, which is degassed, and further implying limited passive degassing between eruptions. Prior to the 1990 eruption, volatiles accumulating at depth were likely blocked by a plug of crystalline magma from the previous event in 1966 and ~4 million m³ of lake water ([Lesage and Surono, 1995](#); [Vandemeulebrouck et al., 2000](#)), whereas before the 2014 eruption, the volcano was plugged by the 2007 dome ([Global Volcanism Program, 2014](#)). In contrast, between the

1990 eruption and up until 2007 dome, the system appears to have been much more open for gas escape, including two unrest crises ([Figure 7](#) and next section). This included fumarolic activity and two heating crises observed in 1996 and 2001, when the lake water increased in temperature from 35 to 40–~50°C ([Bernard and Mazot, 2004](#)). Hence, the observed post- and inter-eruptive crises between 1990 and 2007 suggest the magma system was partially open, allowing the shallow magma body to further degas volatiles out of the system and thus was not able to accumulate excess fluids.

Our proposed interpretation, that the 1990 and 2014 eruptions resulted from the accumulation of pre-eruptive gas, is similar to that of [Cassidy et al. \(2019\)](#) and [Cassidy et al. \(2016\)](#). However, we do not find evidence for the replenishment of hotter and wetter magma involved in the 2007 dome extrusion. Instead, we propose the 2007 dome was the result of leftover magma from the 1990 eruption that underwent slow ascent and degassing until it extruded as a lava dome. This is possible even if the 2007 magma was likely stored under the same conditions as the 1990 and 2014 magmas before it started slow ascent toward the surface.

5.3 Relating magma storage conditions and transport to the surface with unrest signal

Volcanic unrest at Kelud before and during these three eruptions was monitored using a range of observations and data, including seismicity, deformation, and the chemistry and temperature of the lake. Unrest signals preceding all three events started around 2–3 months before eruption, and included seismic swarms with unrest signals spanning volcano-tectonic, shallow volcanic (VB-type), low frequency, and tremor seismicity ([Lesage and Surono, 1995](#); [Hidayati et al., 2019; 2009](#)). Seismicity rapidly increased (e.g., < 24 h) before the 1990 and 2014 eruptions, and earthquake hypocenters are mostly at shallow depths beneath the crater (<7 km) ([Lesage and Surono, 1995](#); [Hidayati et al., 2019](#)). Sharp increases in lake temperature and input of magmatic volatiles such as Cl⁻ and CO₂ into the lake have also been proposed for the unrest prior to the 1990 and 2007 eruptions ([Vandemeulebrouck et al., 2000](#); [Bernard and Mazot, 2004](#); [Kunrat, 2009](#); [Caudron et al., 2012](#)).

Tiltmeters and interferometric synthetic aperture radar (InSAR) detected changes in local and regional deformation from inflation to rapid deflation, preceding 2014 eruption and 2007 dome extrusion, respectively ([Lubis, 2014](#); [Cassidy et al., 2019](#); [Hidayati et al., 2019](#)). [Lubis \(2014\)](#) analyzed InSAR images of the 2007 dome extrusion and detected inflation 1–2 months before the dome extrusion, where they further interpreted the inflation as due to an increase in volume of magma in a shallow reservoir and magma migration to the surface. Tiltmeters from two stations installed at Kelud recorded inflation in the radial and

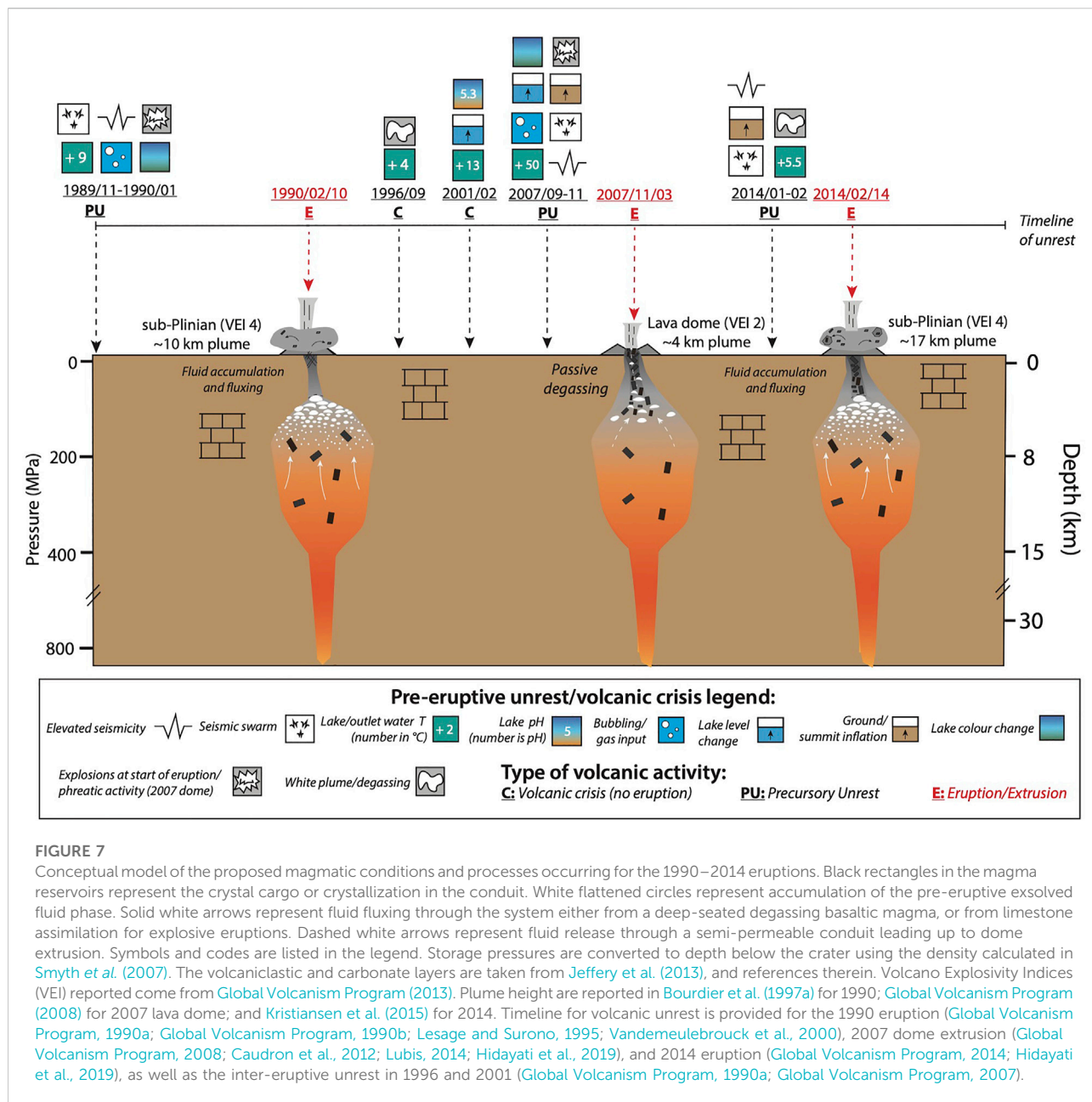


FIGURE 7

Conceptual model of the proposed magmatic conditions and processes occurring for the 1990–2014 eruptions. Black rectangles in the magma reservoirs represent the crystal cargo or crystallization in the conduit. White flattened circles represent accumulation of the pre-eruptive exsolved fluid phase. Solid white arrows represent fluid fluxing through the system either from a deep-seated degassing basaltic magma, or from limestone assimilation for explosive eruptions. Dashed white arrows represent fluid release through a semi-permeable conduit leading up to dome extrusion. Symbols and codes are listed in the legend. Storage pressures are converted to depth below the crater using the density calculated in Smyth et al. (2007). The volcanoclastic and carbonate layers are taken from Jeffery et al. (2013), and references therein. Volcano Explosivity Indices (VEI) reported come from Global Volcanism Program (2013). Plume height for volcanic unrest is provided for the 1990 eruption (Global Volcanism Program, 1990a; Global Volcanism Program, 1990b; Lesage and Surono, 1995; Vandemeulebrouck et al., 2000), 2007 dome extrusion (Global Volcanism Program, 2008; Caudron et al., 2012; Lubis, 2014; Hidayati et al., 2019), and 2014 eruption (Global Volcanism Program, 2014; Hidayati et al., 2019), as well as the inter-eruptive unrest in 1996 and 2001 (Global Volcanism Program, 1990a; Global Volcanism Program, 2007).

tangential directions in January 2014; rapid inflation was also recorded after a M4.5 volcano-tectonic earthquake was recorded in Blitar/Kediri (Hidayati et al., 2019). These observations both record inflation at least 1 month before the 2007 and 2014 eruptions.

An important observation is that during the inter-eruptive period between 1990 and 2007, the system seems to have been able to degas more freely. This is reflected in the volcanic crises that occurred in 1996 and 2001, when lake temperature increased by +4 and +13°C, respectively (Global Volcanism Program, 1990a; Global Volcanism Program, 2007) (Figure 7). Other unrest signals included white plumes (1996), lake

pH decrease, and lake level increase (2001). These releases of heat/mass may represent purging of outgassed magmatic fluids. The 2007 magma would then have lost some of its volatile content, aiding final extrusion in an effusive manner. Given the high crystal content (70 vol%) and complex zoning observed in the crystal cargo, including oscillatory zoning of plagioclase, the lava dome was likely a residual magma batch from the 1990 eruption or earlier. Indeed, we find that the syn-extrusive 2007 dome SO₂ emissions amounted to 0.6–0.7 kT, which is about 1,000 times lower than the 1990 and 2014 eruptions (150 and 200–300 kT, respectively) (Table 6). The low water content is also established in the experiments,

which showed the 2007 magma had at most ~1 wt% water in the melt. Due to frequent cloud cover and the relatively short atmospheric lifetime of SO₂ in the tropics, the OMI satellite measurements of syn-extrusive 2007 dome SO₂ emissions are likely underestimates of actual emissions. However, even in the unlikely event that Kelud had degassed SO₂ continuously throughout the period of most active lava dome growth (November 2007—January 2008; [Global Volcanism Program, 2013](#)) at similar levels to those observed by OMI in November 2007, total SO₂ emissions would only have amounted to ~9 kT; that is, still two orders of magnitude lower than the 1990 and 2014 eruptions. We are therefore confident that the syn-extrusive 2007 lava dome emissions were significantly poorer in SO₂ than the 1990 and 2014 eruptions.

If our hypothesis is correct, identifying and tracking whether a volcanic system is opened or closed to volcanic gases escaping could be useful to anticipate its likely eruptive style. A key component could therefore be to monitor for several unrest signals linked to volcanic gas escape from the magma, and changes to conduit permeability. This includes increased fumarolic activity, decreases in the pH of the lake water, visible upwelling and bubbling, increasing lake temperature, hydroacoustic signals, and clusters of VB-type seismicity ([Lesage and Surono, 1995](#); [Vandemeulebrouck et al., 2000](#); [Bernard and Mazot, 2004](#); [Hidayati, 2009](#)). These unrest signals could suggest the impending eruption would be effusive. On the contrary, monitoring signals that could be related to fluid accumulation and magma degassing, or magma transfer within the plumbing system, could be useful in anticipating explosive eruptions. For example, identification of deep-long period seismicity using broadband seismometers, which could come from degassing of volatile-rich magma at depth ([Melnik and Sparks, 2002](#)) or deformation signals before and after the eruption ([Spang et al., 2022](#)). Finally, microgravity surveys or continuous gravity monitoring could be beneficial because we expect that significant fluid accumulation would lead to subtle changes in density of the plumbing system over time, which was demonstrated at Masaya volcano (Nicaragua) ([Williams-Jones et al., 2003](#)).

6 Conclusion

We present petrological and experimental constraints under the pre-eruptive storage conditions of the basaltic andesite magma feeding the 1990, 2007, and 2014 eruptions of Kelud volcano, which alternated between explosive → effusive → explosive eruption styles. The three eruptions share similar whole rock compositions and mineralogy, implying that their magma storage conditions were also similar. We found that the natural phenocryst content and mineral assemblage can be experimentally reproduced at 975 ± 39°C, 175 ± 25 MPa (~7 km below the crater level), NNO, and with ca. 4–6 wt% water in the melt. We also infer that the 1990 and 2014 magmas co-existed with an exsolved volatile phase under pre-eruptive conditions and propose that this played a main

role to their explosive style. Our mass balance of SO₂ suggests the magma that led to the 2007 lava dome had no or negligible excess fluids. This is likely the result of several inter-eruptive crises after the 1990 eruption that likely allowed gases to be released. Thus, tracking the degree to which volcanoes may be opened or closed to gases escaping in inter-eruptive periods may help to anticipate eruption styles.

Data availability statement

The original contributions presented in the study are included in the article/[Supplementary Material](#), and stored in the data repository of Nanyang Technological University, Singapore (DR-NTU).

Author contributions

SU: conceptualization, project administration, funding acquisition, formal analyses, investigation, data curation, visualization, and writing (original draft; review and editing). JA: methodology, investigation, formal analyses, resources, writing—review and editing, supervision, and final approval of manuscript. FC: conceptualization, investigation, resources, methodology, writing—review and editing, supervision, project administration, funding acquisition, and final approval of manuscript. BS: methodology, writing—review and editing, supervision, funding acquisition, and final approval of manuscript. HH: supervision, writing—review and editing, and final approval of manuscript. SC: analyses, writing—review and editing, and final approval of manuscript.

Funding

JA and BS acknowledge support from both LabEx VOLTAIRE (ANR-10-LABX-100-01) and EquipEx PLANEX (ANR-11-EQPX-0036) projects. SU acknowledges funding from the Stephen Riady Geosciences Scholarship 2018–2019. FC acknowledges support by the Earth Observatory of Singapore *via* its funding from the National Research Foundation Singapore and the Singapore Ministry of Education under the Research Centres of Excellence initiative. FC was funded by NRFi Award (NRFNRFI2017-06). This work comprises EOS contribution number 455. SC acknowledges funding from the NASA Interdisciplinary Research in Earth Science program (80NSSC20K1773).

Acknowledgments

We would like to thank R. Champallier and I. di Carlo from ISTO-Orléans for assistance with experiments and sensor analyses.

Y-J Hsu and J. Oalman from the Earth Observatory of Singapore are thanked for assistance with analyses on the analytical procedures and discussions around experimental petrology. We thank S. Jenkins, C. Widiwijayanti, P. Lesage, and P. Allard for discussions on Kelud volcano. We also thank K. Iacovino for assistance with understanding VESICAL v.1.0.1. We would like to acknowledge the Facility for Analysis, Characterization, Testing and Simulation, Nanyang Technological University, Singapore, for the use of their electron microscopy/X-ray facilities.

Conflict of interest

The authors declare that the research was conducted in the absence of any commercial or financial relationships that could be construed as a potential conflict of interest.

References

- Albarede, F. (1995). *Introduction to geochemical modeling*. Cambridge: Cambridge University Press.
- Andújar, J., Costa, F., and Scaillet, B. (2013). Storage conditions and eruptive dynamics of central versus flank eruptions in volcanic islands: The case of tenerife (canary islands, Spain). *J. Volcanol. Geotherm. Res.* 260, 62–79. doi:10.1016/j.jvolgeores.2013.05.004
- Andersen, D. J., Lindsley, D. H., and Davidson, P. M. (1993). QUILF: A pascal program to assess equilibria among Fe-Mg-Mn-Ti oxides, pyroxenes, olivine, and quartz. *Comput. Geosci.* 19 (9), 1333–1350.
- Arzilli, F., Morgavi, D., Petrelli, M., Polacci, M., Burton, M., Di Genova, D., et al. (2019). The unexpected explosive sub-Plinian eruption of Calbuco volcano (22–23 April 2015; southern Chile): Triggering mechanism implications. *J. Volcanol. Geotherm. Res.* 378, 35–50. doi:10.1016/j.jvolgeores.2019.04.006
- Bernard, A., Knittel, U., Weber, B., Weis, D., Albrecht, A., Hattori, K., et al. (1996). "Petrology and geochemistry of the 1991 eruption products of Mount Pinatubo," in *FIRE and MUD: Eruptions and lahars of mount Pinatubo, Philippines*. Editors C. G. Newhall and R. S. Punongbayan (Seattle, Washington: Univ of Washington Press).
- Bernard, A., and Mazot, A. (2004). "Geochemical evolution of the young crater lake of Kelud volcano in Indonesia," in *Water-rock interaction (WRI-11)*. Editors R. B. Wanty (Rotterdam, Netherlands: A.A. Balkema), 87–90.
- Bourdier, J. L., Pratomo, I., Thouret, J. C., Georges Boudon, G., and Vincent, P. M. (1997a). Observations, stratigraphy and eruptive processes of the 1990 eruption of Kelud volcano, Indonesia. *J. Volcanol. Geotherm. Res.* 79, 181–203. doi:10.1016/s0377-0273(97)00031-0
- Bourdier, J. L., Thouret, J. C., Pratomo, I., Vincent, P. M., and Boudon, G. (1997b). Menaces volcaniques au Kelut (Java, indonésie) : Les enseignements de l'éruption de 1990. *Comptes Rendus de l'Académie des Sci. - Ser. IIA - Earth Planet. Sci.* 324, 961–968. doi:10.1016/s1251-8050(97)83980-8
- Bull, K. F., and Buurman, H. (2013). An overview of the 2009 eruption of Redoubt Volcano, Alaska. *J. Volcanol. Geotherm. Res.* 259, 2–15. doi:10.1016/j.jvolgeores.2012.06.024
- Bucholz, C. E., Gaetani, G. A., Behn, M. D., and Shimizu, N. (2013). Post-entrapment modification of volatiles and oxygen fugacity in olivine-hosted melt inclusions. *Earth Planet. Sci. Lett.* 374, 145–155.
- Campagnola, S., Romano, C., Mastin, L. G., and Vona, A. (2016). Confort 15 model of conduit dynamics: Applications to pantelleria green tuff and etna 122 BC eruptions. *Contributions Mineralogy Petrology* 171, 1–25. doi:10.1007/s00410-016-1265-5
- Caricchi, L., Sheldrake, T. E., and Blundy, J. (2018). Modulation of magmatic processes by CO₂ flushing. *Earth Planet. Sci. Lett.* 491, 160–171. doi:10.1016/j.epsl.2018.03.042
- Carn, S. A., Clarisse, L., and Prata, A. J. (2016). Multi-decadal satellite measurements of global volcanic degassing. *J. Volcanol. Geotherm. Res.* 311, 99–134. doi:10.1016/j.jvolgeores.2016.01.002
- Carn, S. A., Fioletov, V. E., McLinden, C. A., Li, C., and Krotkov, N. A. (2017). A decade of global volcanic SO₂ emissions measured from space. *Sci. Rep.* 7, 44095. doi:10.1038/srep44095
- Carn, S. A. (2022). *Multi-satellite volcanic sulfur dioxide LA long-term global database V4*. Greenbelt, MD, United States: Goddard Earth Science Data and Information Services Center (GES DISC).
- Cashman, K. v., and Sparks, R. J. (2013). How volcanoes work: A 25 year perspective. *Geol. Soc. Am. Bull.* 125, 664–690. doi:10.1130/b30720.1
- Cassidy, M., Castro, J. M., Helo, C., Troll, V. R., Deegan, F. M., Muir, D., et al. (2016). Volatile dilution during magma injections and implications for volcano explosivity. *Geology* 44, 1027–1030. doi:10.1130/g38411.1
- Cassidy, M., Ebmeier, S. K., Helo, C., Watt, S. F. L., Caudron, C., Odell, A., et al. (2019). Explosive eruptions with little warning: Experimental petrology and volcano monitoring observations from the 2014 eruption of Kelud, Indonesia. *Geochem. Geophys. Geosystems*, 1, 30. doi:10.1029/2018gc008161
- Cassidy, M., Manga, M., Cashman, K., and Bachmann, O. (2018). Controls on explosive-effusive volcanic eruption styles. *Nat. Commun.* 9, 3. doi:10.1038/s41467-018-05293-3
- Caudron, C., Mazot, A., and Bernard, A. (2012). Carbon dioxide dynamics in Kelud volcanic lake. *J. Geophys. Res. Solid Earth* 117, 5102. doi:10.1029/2011jb008806
- Corsaro, R. A., and Pompilio, M. (2004). Buoyancy-controlled eruption of magmas at Mt Etna. *Terra nova*. 16, 16–22. doi:10.1046/j.1365-3121.2003.00520.x
- Costa, F., Scaillet, B., and Pichavant, M. (2004). Petrological and experimental constraints on the pre-eruption conditions of holocene dacite from volcan san pedro (36 S, Chilean andes) and the importance of sulphur in silicic subduction-related magmas. *J. Petrology* 45, 855–881. doi:10.1093/petrology/egg114
- Deegan, F. M., Troll, V. R., Freda, C., Misiti, V., Chadwick, J. P., McLeod, C. L., et al. (2010). Magma-carbonate interaction processes and associated CO₂ release at Merapi volcano, Indonesia: Insights from experimental petrology. *J. Petrology* 51, 1027–1051. doi:10.1093/petrology/egq010
- Deegan, F. M., Troll, V. R., Whitehouse, M. J., Jolis, E. M., and Freda, C. (2016). Boron isotope fractionation in magma via crustal carbonate dissolution. *Sci. Rep.* 6, 1–7. doi:10.1038/srep30774
- Deer, W. A., Howie, R. A., and Zussman, J. (1992). *An introduction to the rock-forming minerals*. 2nd ed. Harlow, Essex, England: Longman Scientific & Technical.
- Dingwell, D. B., Bagdassarov, N. S., Bussod, G. Y., and Webb, S. L. (1993). "Magma rheology," in *Experiments at high pressure and applications to the earth's mantle: Short course handbook*. Editor R. W. Luth (Edmonton: Mineralogical Association of Canada), 131–196.
- Dixon, J. E. (1997). Degassing of alkalic basalts. *Am. Mineralogist* 82, 368–378. doi:10.2138/am-1997-3-415
- Edmonds, M., and Woods, A. W. (2018). Exsolved volatiles in magma reservoirs. *J. Volcanol. Geotherm. Res.* 368, 13–30. doi:10.1016/j.jvolgeores.2018.10.018

Publisher's note

All claims expressed in this article are solely those of the authors and do not necessarily represent those of their affiliated organizations, or those of the publisher, the editors, and the reviewers. Any product that may be evaluated in this article, or claim that may be made by its manufacturer, is not guaranteed or endorsed by the publisher.

Supplementary material

The Supplementary Material for this article can be found online at: <https://www.frontiersin.org/articles/10.3389/feart.2022.882097/full#supplementary-material>

- Elissondo, M., Baumann, V., Bonadonna, C., Pistolesi, M., Cioni, R., Bertagnini, A., et al. (2016). Chronology and impact of the 2011 cordón Caulle eruption, Chile. *Nat. Hazards Earth Syst. Sci.* 16, 675–704. doi:10.5194/nhess-16-675-2016
- Erdmann, S., Martel, C., Pichavant, M., Bourdier, J.-L., Champallier, R., Komorowski, J.-C., et al. (2016). Constraints from phase equilibrium experiments on pre-eruptive storage conditions in mixed magma systems: A case study on crystal-rich basaltic andesites from mount Merapi, Indonesia. *J. Petrol.* 57, 535–560. doi:10.1093/petrology/egw019
- Ghiorso, M. S., and Gualda, G. A. R. (2015). An H₂O-CO₂ mixed fluid saturation model compatible with rhyolite-MELTS. *Contrib. Mineral. Pet.* 169, 53. doi:10.1007/s00410-015-1141-8
- Giordano, D., Russell, J. K., and Dingwell, D. B. (2008). Viscosity of magmatic liquids: A model. *Earth Planet. Sci. Lett.* 271, 123–134. doi:10.1016/j.epsl.2008.03.038
- Giuffrida, M., Holtz, F., Vetere, F., and Viccaro, M. (2017). Effects of CO₂ flushing on crystal textures and compositions: Experimental evidence from recent K-trachybasalts erupted at Mt. Etna. *Contributions Mineralogy Petrology* 172, 1–18. doi:10.1007/s00410-017-1408-3
- Global Volcanism Program (GVP) (2013). Kelut (Kelud). Report.
- Global Volcanism Program (GVP) (1990b). Report on Kelut (Indonesia) 15. Report.
- Global Volcanism Program (GVP) (1990a). Report on Kelut (Indonesia). Report. Bull. Glob. Volcanism Netw.
- Global Volcanism Program (GVP) (2007). Report on Kelut (Indonesia). Report. Bulletin of the Global Volcanism Network.
- Global Volcanism Program (GVP) (2008). Report on Kelut (Indonesia) 33. Report.
- Global Volcanism Program (GVP) (2014). Report on Kelut (Indonesia) 39. Report.
- Gonnermann, H. M., and Manga, M. (2013). “Dynamics of magma ascent in the volcanic conduit,” in *Modeling volcanic processes: The physics and mathematics of volcanism*. Editors S. Fagents, T. K. P. Gregg, and R. M. C. Lopes (Cambridge University Press), 55–84. doi:10.1017/cbo9781139021562.004
- Hidayati, S., Basuki, A., and KristiantoMulyana, I. (2009). Emergence of lava dome from the crater lake of Kelud volcano. *East Java* 4, 229–238. doi:10.17014/ijog.v4i4.83
- Hidayati, S. (2009). Emergence of lava dome from the crater lake of Kelud volcano, East Java. *Indonesian J. Geoscience* 4, 229–238. doi:10.17014/ijog.vol4no4.20091
- Hidayati, S., Triastuty, H., Mulyana, I., Adi, S., Ishihara, K., Basuki, A., et al. (2019). Differences in the seismicity preceding the 2007 and 2014 eruptions of Kelud volcano, Indonesia. *J. Volcanol. Geotherm. Res.* 382, 50–67. doi:10.1016/j.jvolgeores.2018.10.017
- Humaida, H. (2013). *A geochemical study on Merapi and Kelud volcanic eruptions* (Unpublished PhD Thesis). Yogyakarta, Indonesia: Universitas Gadjah Mada.
- Iacovino, K., Matthews, S., Wieser, P. E., Moore, G. M., and Bégue, F. (2021). VESCAL Part I: An open-source thermodynamic model engine for mixed volatile (H₂O-CO₂) solubility in silicate melts. *Earth Space Sci.* 8, 1–55. doi:10.1029/2020ea001584
- Jay, J., Costa, F., Pritchard, M., Lara, L., Singer, B., and Herrin, J. (2014). Locating magma reservoirs using InSAR and petrology before and during the 2011–2012 Cordón Caulle silicic eruption. *Earth Planet. Sci. Lett.* 395, 254–266. doi:10.1016/j.epsl.2014.03.046
- Jeffery, A. J., Gertisser, R., Troll, V. R., Jolis, E. M., Dahren, B., Harris, C., et al. (2013). The pre-eruptive magma plumbing system of the 2007–2008 dome-forming eruption of Kelut volcano, East Java, Indonesia. *Contrib. Mineral. Pet.* 166, 275–308. doi:10.1007/s00410-013-0875-4
- Kristiansen, N. I., Prata, A. J., Stohl, A., and Carn, S. A. (2015). Stratospheric volcanic ash emissions from the 13 February 2014 Kelut eruption. *Geophys. Res. Lett.* 42, 588–596. doi:10.1002/2014gl02307
- Kunrat, S. L. (2009). *Geochemical and thermodynamic modeling of volcanic fluids and their interpretation for volcano monitoring* (Unpublished MSc thesis). Brussels, Belgium: Université Libre de Bruxelles.
- Lê, S., Josse, J., and Husson, F. (2008). FactoMineR: An R package for multivariate analysis. *J. Stat. Softw.* 25, 1–18. doi:10.18637/jss.v025.i01
- Leake, B. E., Woolley, A. R., Arps, C. E. S., Birch, W. D., Gilbert, M. C., Grice, J. D., et al. (1997). Nomenclature of amphiboles report of the subcommittee on amphiboles of the international mineralogical association commission on new minerals and mineral names. *ejm* 9, 623–651. doi:10.1127/ejm/9/3/0623
- Lesage, P., and Suroño (1995). Seismic precursors of the february 10, 1990 eruption of Kelut volcano, Java. *J. Volcanol. Geotherm. Res.* 65, 135–146. doi:10.1016/0377-0273(94)00051-h
- Li, C., Krotkov, N. A., Carn, S. A., Zhang, Y., Spurr, R. J. D., and Joiner, J. (2017). New-generation NASA Aura Ozone monitoring instrument (OMI) volcanic SO₂ dataset: Algorithm description, initial results, and continuation with the suomi-NPP Ozone mapping and profiler suite (OMPS). *Atmos. Meas. Tech.* 10, 445–458. doi:10.5194/amt-10-445-2017
- Li, W., Costa, F., and Nagashima, K. (2021). Apatite crystals reveal melt volatile budgets and magma storage depths at Merapi volcano, Indonesia. *J. Petrology* 62, egaa100. doi:10.1093/petrology/egaa100
- Longpré, M. A., Stix, J., Costa, F., Espinoza, E., and Muñoz, A. (2014). Magmatic processes and associated timescales leading to the January 1835 eruption of Cosigüina Volcano, Nicaragua. *J. Petrology* 55, 1173–1201. doi:10.1093/petrology/egu022
- Lubis, A. M. (2014). Uplift of Kelud volcano prior to the november 2007 eruption as observed by L-band insar. *J. Eng. Technol. Sci.* 46, 245–257. doi:10.5614/j.eng.technol.sci.2014.46.3.1
- Maeno, F., Nakada, S., Yoshimoto, M., Shimano, T., Hokanishi, N., Zaennudin, A., et al. (2019a). A sequence of a plinian eruption preceded by dome destruction at Kelud volcano, Indonesia, on February 13, 2014, revealed from tephra fallout and pyroclastic density current deposits. *J. Volcanol. Geotherm. Res.* 382, 24–41. doi:10.1016/j.jvolgeores.2017.03.002
- Maeno, F., Nakada, S., Yoshimoto, M., Shimano, T., Hokanishi, N., Zaennudin, A., et al. (2019b). Eruption pattern and a long-term magma discharge rate over the past 100 years at Kelud Volcano, Indonesia. *J. Disaster Res.* 14, 27–39. doi:10.20965/jdr.2019.p0027
- Martel, C. (2012). Eruption dynamics inferred from microlite crystallization experiments: Application to plinian and dome-forming eruptions of Mt. Pelee (Martinique, lesser antilles). *J. Petrology* 53, 699–725. doi:10.1093/petrology/egr076
- Mastin, L. G. (2002). Insights into volcanic conduit flow from an open-source numerical model. *Geochem. Geophys. Geosystems* 3, 229–235. doi:10.1029/2001gc000192
- Melnik, O., and Sparks, R. S. J. (2002). “Modelling of conduit flow dynamics during explosive activity at Soufrière Hills Volcano, Montserrat,” in *Geological society* (London: Geological Society Publications), 21, 307–317. doi:10.1144/gsl.mem.2002.21.01.14Memoirs
- Melnik, O., and Sparks, R. S. J. (1999). Nonlinear dynamics of lava dome extrusion. *Nature* 402, 37–41. doi:10.1038/46950
- Nakamichi, H., Iguchi, M., Triastuty, H., Hendrasto, M., and Mulyana, I. (2017). Differences of precursory seismic energy release for the 2007 effusive dome-forming and 2014 Plinian eruptions at Kelud volcano, Indonesia. *J. Volcanol. Geotherm. Res.* 15, 68–80. doi:10.1016/j.jvolgeores.2017.08.004
- Nakashima, Y., Heki, K., Takeo, A., Cahyadi, M. N., Aditya, A., and Yoshizawa, K. (2016). Atmospheric resonant oscillations by the 2014 eruption of the Kelud volcano, Indonesia, observed with the ionospheric total electron contents and seismic signals. *Earth Planet. Sci. Lett.* 434, 112–116. doi:10.1016/j.epsl.2015.11.029
- Norrish, K., and Hutton, J. T. (1969). An accurate X-ray spectrographic method for the analysis of a wide range of geological samples. *Geochimica Cosmochimica Acta* 33, 431–453. doi:10.1016/0016-7037(69)90126-4
- Pallister, J. S., Hoblitt, R. P., Crandell, D. R., and Mullineaux, D. R. (1992). Mount St. Helens a decade after the 1980 eruptions: Magmatic models, chemical cycles, and a revised hazards assessment. *Bull. Volcanol.* 54, 126–146. doi:10.1007/bf00278003
- Pallister, J. S., Hoblitt, R. P., Meeker, G. P., Knight, R. J., and Siems, D. F. (1996). “Magma mixing at mount Pinatubo: Petrographic and chemical evidence from the 1991 deposits,” in *FIRE and MUD: Eruptions and lahars of mount Pinatubo, Philippines*. Editors C. G. Newhall and R. S. Punongbayan (Seattle, Washington: Univ of Washington Press).
- Pichavant, M., Costa, F., Burgisser, A., Scaillet, B., Martel, C., and Poussineau, S. (2007). Equilibration scales in silicic to intermediate magmas implications for experimental studies. *J. Petrology* 48, 1955–1972. doi:10.1093/petrology/egm045
- Pichavant, M., Martel, C., Bourdier, J.-L., and Scaillet, B. (2002). Physical conditions, structure, and dynamics of a zoned magma chamber: Mount Pelée (Martinique, Lesser Antilles Arc). *J. Geophys. Res.* 107, 1–28. doi:10.1029/2001jb000315
- Popa, R. G., Dietrich, V. J., and Bachmann, O. (2020). Effusive-explosive transitions of water-undersaturated magmas. The case study of methana volcano, south aegean arc. *J. Volcanol. Geotherm. Res.* 399, 106884. doi:10.1016/j.jvolgeores.2020.106884
- Popa, R. G., Tollan, P., Bachmann, O., Schenker, V., Ellis, B., and Allaz, J. M. (2021). Water exsolution in the magma chamber favors effusive eruptions: Application of Cl-F partitioning behavior at the Nisyros-Yali volcanic area. *Chem. Geol.* 570, 120170. doi:10.1016/j.chemgeo.2021.120170

- Pownceby, M. I., and O'Neill, H. S. C. (1994). Thermodynamic data from redox reactions at high temperatures. IV. Calibration of the Re-ReO₂ oxygen buffer from EMF and NiO+Ni-Pd redox sensor measurements. *Contr. Mineral. Pet.* 118, 130–137. doi:10.1007/bf01052864
- Prouteau, G., and Scaillet, B. (2003). Experimental constraints on the origin of the 1991 Pinatubo dacite. *J. Petrology* 44, 2203–2241. doi:10.1093/ptrology/egg075
- Putirka, K. (2016). Amphibole thermometers and barometers for igneous systems and some implications for eruption mechanisms of felsic magmas at arc volcanoes. *Am. Mineralogist* 101, 841–858. doi:10.2138/am-2016-5506
- Putirka, K. D. (2008). Thermometers and barometers for volcanic systems. *Rev. Mineralogy Geochem.* 69, 61–120. doi:10.2138/rmg.2008.69.3
- Ridolfi, F., Renzulli, A., and Puerini, M. (2010). Stability and chemical equilibrium of amphibole in calc-alkaline magmas: An overview, new thermobarometric formulations and application to subduction-related volcanoes. *Contrib. Mineral. Pet.* 160, 45–66. doi:10.1007/s00410-009-0465-7
- Roux, J., and Lefèvre, A. (1992). A fast-quench device for internally heated pressure vessels. *ejm* 4, 279–282. doi:10.1127/ejm/4/2/0279
- Scaillet, B., and Evans, B. W. (1999). The 15 June 1991 eruption of mount Pinatubo. I. Phase equilibria and pre-eruption P-T-fO₂-fH₂O conditions of the dacite magma. *J. Petrology* 40, 381–411. doi:10.1093/ptroj/40.3.381
- Scaillet, B., Pichavant, M., and Roux, J. (1995). Experimental crystallization of leucogranite magmas. *J. Petrology* 36, 663–705. doi:10.1093/ptrology/36.3.663
- Scaillet, B., Pichavant, M., Roux, J., Humbert, G., and Lefèvre, A. (1992). Improvements of the Shaw membrane technique for measurement and control of fH₂ at high temperatures and pressures. *Am. Mineralogist* 77, 647–655.
- Shinohara, H. (2008). Excess degassing from volcanoes and its role on eruptive and intrusive activity. *Rev. Geophys.* 46, 1–31. doi:10.1029/2007rg000244
- Shishkina, T. A., Botcharnikov, R. E., Holtz, F., Almeev, R. R., and Portnyagin, M. V. (2010). Solubility of H₂O- and CO₂-bearing fluids in tholeiitic basalts at pressures up to 500MPa. *Chem. Geol.* 277, 115–125. doi:10.1016/j.chemgeo.2010.07.014
- Sisson, T. W., and Bacon, C. R. (1999). Gas-driven filter pressing in magmas. *Geol* 27, 613–616. doi:10.1130/0091-7613(1999)027<0613:gdfpim>2.3.co;2
- Smyth, H. R., Hamilton, P. J., Hall, R., and Kinny, P. D. (2007). The deep crust beneath island arcs: Inherited zircons reveal a gondwana continental fragment beneath East Java, Indonesia. *Earth Planet. Sci. Lett.* 258, 269–282. doi:10.1016/j.epsl.2007.03.044
- Spang, A., Burton, M., Kaus, B. J. P., and Sigmundsson, F. (2022). Quantification of volcano deformation caused by volatile accumulation and release. *Geophys. Res. Lett.* 49, 1–10. doi:10.1029/2021gl097502
- Surono, Jousset, P., Pallister, J., Boichu, M., Buongiorno, M. F., Budisantoso, A., et al. (2012). The 2010 explosive eruption of Java's Merapi volcano-A '100-year' event. *J. Volcanol. Geotherm. Res.* 241–242, 121–135. doi:10.1016/j.jvolgeores.2012.06.018
- Tait, S., Jaupart, C., and Vergnolle, S. (1989). Pressure, gas content and eruption periodicity of a shallow, crystallising magma chamber. *Earth Planet. Sci. Lett.* 92, 107–123. doi:10.1016/0012-821x(89)90025-3
- Taylor, J. R., Wall, V. J., and Pownceby, M. I. (1992). The calibration and application of accurate redox sensors. *Am. Mineralogist* 77, 284–295.
- Thouret, J.-C., Abdurachman, K. E., Bourdier, J.-L., and Bronto, S. (1998). Origin, characteristics, and behaviour of lahars following the 1990 eruption of Kelud volcano, eastern Java (Indonesia). *Bull. Volcanol.* 59, 460–480. doi:10.1007/s004450050204
- Tramontano, S., Gualda, G. A. R., and Ghiorsio, M. S. (2017). Internal triggering of volcanic eruptions: Tracking overpressure regimes for giant magma bodies. *Earth Planet. Sci. Lett.* 472, 142–151. doi:10.1016/j.epsl.2017.05.014
- Utami, S. B., Costa, F., Lesage, P., Allard, P., and Humaida, H. (2021). Fluid fluxing and accumulation drive decadal and short-lived explosive basaltic andesite eruptions preceded by limited volcanic unrest. *J. Petrology* 62, egab086. doi:10.1093/ptrology/egab086
- Utami, S. B. (2021). *Petrological and monitoring insights into the mechanisms driving eruptions of Kelud volcano, Indonesia (Unpublished PhD Thesis)*. Singapore: Nanyang Technological University.
- Vandemeulebrouck, J., Sabroux, J.-C., Halbwegs, M., Surono, N., Poussielgue, J., Grangeon, J., et al. (2000). Hydroacoustic noise precursors of the 1990 eruption of Kelut Volcano, Indonesia. *J. Volcanol. Geotherm. Res.* 97, 443–456. doi:10.1016/s0377-0273(99)00176-6
- Waters, L. E., and Lange, R. A. (2017). An experimental study of Fe²⁺-MgKD between orthopyroxene and rhyolite: A strong dependence on H₂O in the melt. *Contributions Mineralogy Petrology* 172, 1–13. doi:10.1007/s00410-017-1358-9
- Waters, L. E., and Lange, R. A. (2015). An updated calibration of the plagioclase-liquid hygrometer-thermometer applicable to basalts through rhyolites. *Am. Mineralogist* 100, 2172–2184. doi:10.2138/am-2015-5232
- Whelley, P. L., Newhall, C. G., and Bradley, K. E. (2015). The frequency of explosive volcanic eruptions in Southeast Asia. *Bull. Volcanol.* 77, 1. doi:10.1007/s00445-014-0893-8
- Williams-Jones, G., Rymer, H., and Rothery, D. A. (2003). Gravity changes and passive SO₂ degassing at the Masaya caldera complex, Nicaragua. *J. Volcanol. Geotherm. Res.* 123, 137–160. doi:10.1016/s0377-0273(03)00033-7
- Wirakusumah, A. D. (1991). *Some studies of volcanology, petrology and structure of Mt. Kelut, east Java, Indonesia (Unpublished PhD Thesis)*. Wellington, New Zealand: Victoria University of Wellington.
- Woods, A. W., and Koyaguchi, T. (1994). Transitions between explosive and effusive eruptions of silicic magmas. *Nature* 370, 641–644. doi:10.1038/370641a0
- Young, S. R., Sparks, R. S. J., Aspinall, W. P., Lynch, L. L., Miller, A. D., Robertson, R. E. A., et al. (1998). Overview of the eruption of soufriere Hills volcano, Montserrat, 18 July 1995 to december 1997. *Geophys. Res. Lett.* 25, 3389–3392. doi:10.1029/98gl01405
- Zhu, Y., Toon, O. B., Jensen, E. J., Bardeen, C. G., Mills, M. J., and Tolbert, M. A. (2020). Persisting volcanic ash particles impact stratospheric SO₂ lifetime and aerosol optical properties. *Nat. Com.* 11 (1), 1–11.